Magnetic interactions and possible structural distortion in kagome FeGe from first-principles calculations and symmetry analysis

Hanjing Zhou,[1,2,*] Songsong Yan,[1,2,*] Dongze Fan,[1,2] Di Wang,[1,2,†] and Xiangang Wan[1,2,3,‡]
[1]*National Laboratory of Solid State Microstructures and School of Physics, Nanjing University, Nanjing 210093, China*
[2]*Collaborative Innovation Center of Advanced Microstructures, Nanjing University, Nanjing 210093, China*
[3]*Hefei National Laboratory, Hefei 230088, China*

(Received 6 December 2022; revised 2 May 2023; accepted 27 June 2023; published 19 July 2023)

Recently, charge density wave (CDW) order has been discovered in a magnetic kagome metal FeGe, providing a platform to explore the possible connection between magnetism and CDW in a kagome lattice. Based on density functional theory and symmetry analysis, we present a comprehensive investigation of electronic structure, magnetic properties, and possible structural distortion of FeGe. We estimate the magnetic parameters including Heisenberg and Dzyaloshinskii-Moriya (DM) interactions, and find that the ferromagnetic nearest-neighbor J_1 dominates over the others, while the magnetic interactions between nearest kagome layers favors antiferromagnetic. The Néel temperature T_N and Curie-Weiss temperature θ_{CW} are successfully reproduced, and the calculated magnetic anisotropy energy is also consistent with the experimental results. However, these reasonable Heisenberg interactions and magnetic anisotropy cannot explain the double cone magnetic transition, and the DM interactions, which even exist in the centrosymmetric materials, can result in this small magnetic cone angle. Unfortunately, due to the crystal symmetry of the high-temperature structure, the net contribution of DM interactions to double cone magnetic structure is absent. Based on the experimental $2 \times 2 \times 2$ supercell, we thus explore the subgroups of the parent phase. Group theoretical analysis reveals that there are 68 different distortions, and only four of them (space group $P622$ or $P6_322$) without inversion and mirror symmetry thus can explain the low-temperature magnetic structure. Furthermore, we suggest that these four proposed CDW phases can be identified by using Raman spectroscopy. Since DM interactions are very sensitive to small atomic displacements and symmetry restrictions, we believe that symmetry analysis is a useful method to reveal the interplay of delicate structural distortions and complex magnetic configurations.

DOI: 10.1103/PhysRevB.108.035138

I. INTRODUCTION

Kagome lattices are emerging as an exciting platform for the rich physics, including magnetism, charge density wave (CDW), topology, and superconductivity [1–43] Three key features have been identified in the electronic structure associated with its lattice geometry, which are flat bands derived from the destructive phase interference of nearest-neighbor hopping, topological Dirac crossing at the K point in the Brillouin zone, and a pair of van Hove singularities (vHSs) at the M point [2–5]. When large density of states from the kagome flat bands are located near the Fermi level, strong electron correlations can induce magnetic order [2,3]. There are several magnetic kagome materials, such as FeSn [6–10], Fe_3Sn_2 [11–14], Mn_3Sn [15], $Co_3Sn_2S_2$ [16], and AMn_6Sn_6 (A=Tb, Y) [17,18], which usually exhibit magnetic order with ferromagnetically ordered layers that are either ferromagnetically or antiferromagnetically stacked. Meanwhile, when vHSs are located near the Fermi level, interaction between the saddle points and lattice instability could induce symmetry-breaking CDW order [4,5], such as the class of recently discovered kagome materials AV_3Sb_5 (A=K, Rb, Cs) [19–41]. Significant interest has been focused on them since an unusual competition between unconventional superconductivity and CDW order has been found [19–41]. Note that in a kagome system, magnetic order and CDW order have not been usually observed simultaneously within one material, probably due to the fact that they originate from the flat band and the vHSs, respectively, which have a large energy difference and usually do not both appear near the Fermi level [44].

Very recently, CDW order was discovered to appear deeply in a magnetically ordered kagome metal FeGe, providing the opportunity for understanding the interplay between CDW and magnetism in a kagome lattice [44–49]. Isostructural to FeSn [6–10] and CoSn [42,43], hexagonal FeGe consists of stacks of Fe kagome planes with both in-plane and interplane Ge atoms [50]. A sequence of magnetic phase transitions have been discussed in the 1970s-80s [51–56]. Below $T_N = 410$ K, FeGe exhibits collinear A-type antiferromagnetic (AFM) order with moments aligned ferromagnetically (FM) within each plane and antialigned between layers, and becomes a c-axis double cone AFM structure at a lower temperature $T_{canting} = 60$ K [55,56]. Recent neutron scattering, spectroscopy, and transport measurements suggest a CDW in FeGe which takes place at T_{CDW} around 100 K, providing the first example of a CDW in a kagome magnet [45,46]. The CDW in FeGe enhances the AFM ordered moment and induces an emergent

*These authors contributed equally to this work.
†Corresponding author: diwang0214@nju.edu.cn
‡Corresponding author: xgwan@nju.edu.cn

anomalous Hall effect (AHE) possibly associated with a chiral flux phase similar with AV_3Sb_5 [34–36], suggesting an intimate correlation between spin, charge, and lattice degree of freedom [45]. Though AHE is not usually seen in antiferromagnets in zero field, recent studies have shown that a breaking of combined time-reversal and lattice symmetries in the AFM state results in the AHE [57–59]. In kagome FeGe, the AHE associated with CDW order indicates that the combined symmetry breaking occurs via the structural distortion or magnetic structure transition below the CDW temperature. The CDW in FeGe was then extensively studied experimentally and theoretically [44–49], and the CDW wave vectors are identical to that of AV_3Sb_5 [23–28]. However, sharply different from AV_3Sb_5 [39–41], all the theoretically calculated phonon frequencies in FeGe remain positive [44,48,49], and the structural distortion of the CDW phase remain elusive. It was suggested to be reduced to $P622$ with the distortion of two nonequivalent Fe atoms [45], while later works proposes that FeGe shares the same space group of $P6/mmm$ with the pristine phase [48,49]. Based on first-principles calculations and scanning tunneling microscopy, Shao *et al*. showed that the CDW phase of FeGe exhibits a generalized Kekulé distortion [60] in the Ge honeycomb atomic layers [48]. Meanwhile, using hard x-ray diffraction and spectroscopy, Miao *et al*. report an experimental discovery of charge dimerization that coexists with the CDW phase in FeGe [49]. Therefore, the understanding of the magnetism and the intertwined connection between complex magnetism and structural distortion in kagome FeGe is an emergency issue, which we will address in this paper based on first-principles study and symmetry analysis.

In this paper, we systematically analyze the electronic and magnetic properties of kagome FeGe. Our numerical results show that this material is a magnetic metal exhibiting large magnetic splitting around 1.8 eV. Based on combining magnetic force theorem and linear-response approach [61–63], the magnetic exchange parameters have been estimated. The results show that the nearest-neighbor J_1 is FM and dominates over the others, while the magnetic interactions between nearest kagome layers favors AFM, consequently resulting in the A-type AFM ground-state configuration. Based on these spin exchange parameters, the calculated Néel temperature and Curie-Weiss temperature also agree well with the experiments. Using the method in Refs. [64,65], we also calculate the magnetic anisotropic energy (MAE) to be around 0.066 meV per Fe atom with easy axis being out of the kagome layers, which is in reasonable agreement with the experimental results [56]. However, the double cone magnetic transition at $T_{\text{canting}} = 60$ K cannot be reproduced by these reasonable magnetic parameters. We find that Dzyaloshinskii-Moriya (DM) interactions [66,67] are much more efficient than Heisenberg interactions for causing this canted spin structure. Unfortunately, the space group $P6/mmm$ of the high-temperature phase in FeGe has inversion symmetry and mirror symmetries, and all of them eliminate the net contribution of DM interactions to the double cone magnetic structure. It is well-known that DM interactions are very sensitive to atomic displacements, while small structural distortion usually has little effect on Heisenberg interactions. Therefore, we explore the possible CDW distortions which can explain the low-temperature magnetic structure. Symmetry theoretical analysis reveals that there are 68 different distortions, which are the subgroups of the parent $P6/mmm$ phase with $2 \times 2 \times 2$ supercell [45,46,48,49]. Based on the group theoretical analysis, we find that only four structures (space groups $P622$ and $P6_322$) without inversion and mirror symmetry thus can have double cone spin structure. We further propose that using Raman spectroscopy, these four CDW phases can be identified from their different numbers of Raman active peaks.

II. METHOD

The first-principles calculations have been carried out by using the full potential linearized augmented plane-wave method as implemented in the WIEN2K package [68]. The k-point mesh convergence test has been done (see Appendix), and $13 \times 13 \times 14$ k-point mesh is used for the Brillouin-zone integral of nonmagnetic structure while $13 \times 13 \times 7$ k-point mesh is used for AFM structure. The self-consistent calculations are considered to be converged when the difference in the total energy does not exceed $0.01m$Ry at consecutive self-consistent steps.

It is well-known that magnetism is computationally tricky and may require the DFT (density functional theory) + DMFT (dynamical mean-field theory) method [69]. However, in many magnetic systems, the mean-field theory such as the local spin-density approximation (LSDA) [70] or LSDA + U schemes could also yield satisfactory results. The LSDA + U scheme with reasonable U is widely applied to the Slater insulator [71], Weyl semimetal [72], and Axion insulator [73]. Meanwhile, we note that the LSDA calculations works well for B20-FeGe, which exhibits a magnetic skyrmion phase [74–76]. Therefore, we believe that the LSDA calculation can also present a reasonable description for the magnetic properties of the kagome FeGe. We also perform the first-principles calculations with different exchange-correlation potentials, and the calculated band structures are almost the same (see Appendix). Furthermore, we also perform the LSDA + U scheme [77] with the value of U varied from 0 to 4 eV. The calculated magnetic moments with $U = 0$ eV are in the best agreement with the experimental results (see Appendix); thus we present the first-principles results from the $U = 0$ eV calculation in the following.

In addition, we include the spin orbit coupling (SOC) [78], which results in the DM interaction. As shown in the following, any reasonable Heisenberg interaction cannot explain the double cone magnetic structure [51–56] and the DM interaction is necessary. The contribution of DM interactions to the low-temperature magnetic structure is restricted by the crystal symmetry, which inspires us to identify the possible CDW structures based on the symmetry analysis, as shown in the following.

The spin exchange interactions, including Heisenberg and DM interactions [66,67], are calculated using first principles based on combining magnetic force theorem and linear-response approach [61–63], which have successfully applied to various magnetic materials [62,63,79–81].

Monte Carlo (MC) simulations are performed with Metropolis algorithm for Heisenberg model [82–84]. The size of the cell in the MC simulation are $16 \times 16 \times 16$-unit cells

TABLE I. Spin exchange parameters (in meV) including Heisenberg and DM interactions of FeGe evaluated from LSDA+SOC calculations, respectively. The Fe-Fe distances and the corresponding number of neighbors (NN) are presented in the second and third columns

	Distance (Å)	NN	J	DM
J_1	2.50	4	−41.97	(0, 0, 0.03)
J_2	4.33	4	5.49	(0, 0, −0.12)
J_{c1}	4.05	2	8.44	(0, 0, 0)
J_{c2}	4.76	8	−2.04	(0.01, −0.02, −0.07)
J_{c3}	5.93	8	1.81	(0.07, −0.04, −0.09)
$J_{c'1}$	8.11	2	−0.66	(0, 0, 0)
$J_{c'2}$	8.49	8	0.09	(−0.04, −0.09, −0.03)

with periodic boundary conditions. The details of the convergence test for cell size are displayed in the Appendix. At each temperature, we carry out 400 000 sweeps to prepare the system, and sample averages are accumulated over 800 000 sweeps.

All the input files for the computational details of the first-principles calculations for band structures, Heisenberg, and DM interactions, as well as MC simulations, can be obtained in the open-source website of Ref. [85].

III. RESULTS

A. The electronic and magnetic properties

The pristine phase of FeGe crystallizes in the hexagonal structure with space group $P6/mmm$ (No. 191) [50], where the coordinates of the atoms are shown in Table II and Fig. 1. First, we perform nonmagnetic local-density approximation (LDA) + SOC calculations, and show the band structures and partial density of states in Figs. 2(a)–2(c). While Ge-$2p$ states are mainly located between −6.0 and −2.0 eV as shown in Fig. 5 of the Appendix, the main contribution around the Fermi level comes from the $3d$ orbitals of Fe ions. Along the high-symmetry directions $\Gamma - M - K - \Gamma$ lying in the $k_z = 0$ plane, there are two different kagome structures near the Fermi level. Consistent with previous first-principles calculations [44,47], the kagome flat bands around the Fermi level exhibit a large peak in the density of states as shown in Fig. 2(c), which indicates magnetic instability. Therefore, LSDA + SOC calculations are performed based on the A-type AFM configuration, and the band structures and partial density of states are shown in Figs. 2(d)–2(f). The magnetic moment of Fe ions is estimated to be 1.55 μ_B, which is in agreement with the previous experimental value around 1.7 μ_B [52,54]. Note that each kagome layer is FM and the key signatures of electronic structures in the kagome lattice remain. The magnetic splitting is around 1.8 eV, which makes the large peaks above and below the Fermi level correspond to the spin minority bands and spin majority bands respectively, as shown in Fig. 2(f). Meanwhile, the vHSs that are relatively far from the Fermi level in the nonmagnetic state [−0.65 eV and −0.76 eV as shown in Figs. 2(a) and 2(b)] are brought near the Fermi level by the spin splitting, as shown in Figs. 2(d) and 2(e). We present orbital-resolved band structures and find that the vHSs near the Fermi level in the A-type AFM configuration, marked as vHS-1 (located at 0.07 eV above fermi energy) and vHS-2 (-0.26 eV) in Figs. 2(d) and 2(e), are mainly contributed by the $d_{xy}/d_{x^2-y^2}$ and d_{xz}/d_{yz} orbitals, respectively. These vHSs near the Fermi level are suggested to induce symmetry-breaking CDW order in kagome metal FeGe [44].

To quantitatively understand the rich magnetic phenomenon in kagome FeGe, a microscopic magnetic model with proper parameters is extremely important. Based on the calculated electronic structures, we estimate the exchange parameters including Heisenberg and DM interactions using the linear-response approach [61–63] and summarize the results in Table I. As shown in Fig. 1, we divide the magnetic interactions considered into three types: the exchange interactions J_i, J_{ci}, and $J_{c'i}$ represent the ith-nearest-neighbor interactions between Fe ions within kagome layers, on the nearest kagome layers, and on the next-nearest kagome layers, respectively. As shown in Table I, the in-plane nearest-neighbor coupling J_1 favors FM order and is estimated to be −41.97 meV, which has a similar value to the one in kagome FeSn (around

TABLE II. Four types of $2 \times 2 \times 2$ CDW phases which can lead to nonzero DM contribution to double cone spin structure. The corresponding Wyckoff positions and the coordinates of the atoms in the pristine phase and these four CDW phases are summarized.

Pristine phase ($P6/mmm$)			$P622$ (type I)			$P622$ (type II)			$P6_322$ (type I)			$P6_322$(type II)		
	WP	Coordinates		WP	Coordinates		WP	Coordinates		WP	Coordinates		WP	Coordinates
Ge1	1a	(0, 0, 0)	Ge1	1a	(0, 0, 0)	Ge1	2e	(0, 0, z_1)	Ge1	2a	(0, 0, 0)	Ge1	2b	(0, 0, 1/4)
			Ge2	1b	(0, 0, 1/2)	Ge2	6i	(1/2, 0, z_2)	Ge2	6g	(x_1, 0, 0)	Ge2	6h	(x_1, 2x_1, 1/4)
			Ge3	3f	(0, 1/2, 0)									
			Ge4	3g	(0, 1/2, 1/2)									
Ge2	2d	(1/3, 2/3, 1/2)	Ge5	4h	(1/3, 2/3, z_1)	Ge3	2c	(1/3, 2/3, 0)	Ge3	2c	(1/3, 2/3, 1/4)	Ge3	4f	(1/3, 2/3, z_2)
			Ge6	12n	(x_2, y_2, z_2)	Ge4	2d	(1/3, 2/3,1/2)	Ge4	2d	(1/3, 2/3, 3/4)	Ge4	12i	(x_3, y_3, z_3)
						Ge5	6l	(x_3, 2x_3, 0)	Ge5	6h	(x_2, 2x_2, 1/4)			
						Ge6	6m	(x_4, 2x_4, 1/2)	Ge6	6h	(x_3, 2x_3, 1/4)			
Fe	3f	(1/2, 0, 0)	Fe1	6j	(x_3, 0, 0)	Fe1	12n	(x_5, y_5, z_5)	Fe1	6g	(x_4, 0, 0)	Fe1	6h	(x_4, 2x_4, 1/4)
			Fe2	6k	(x_4, 0, 1/2)	Fe2	12n	(x_6, y_6, z_6)	Fe2	6g	(x_5, 0, 0)	Fe2	6h	(x_5, 2x_5, 1/4)
			Fe3	6l	(x_5, 2x_5, 0)				Fe3	12i	(x_6, y_6, z_6)	Fe3	12i	(x_6, y_6, z_6)
			Fe4	6m	(x_6, 2x_6, 1/2)									

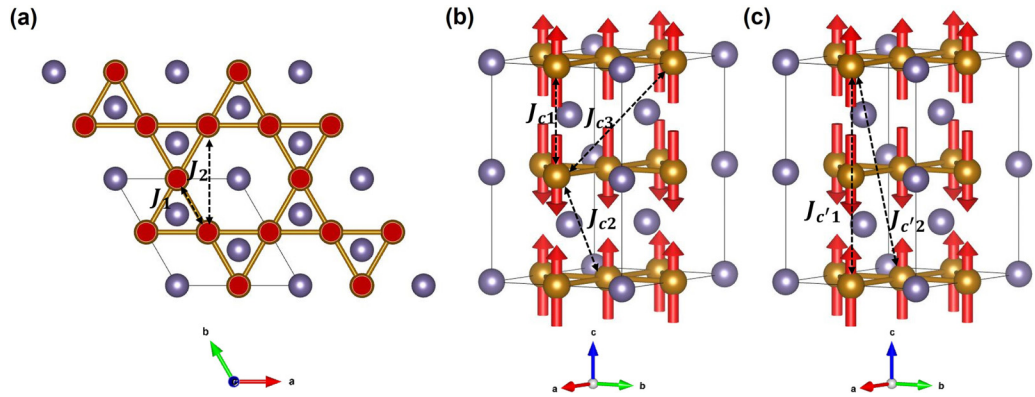

FIG. 1. Crystal and magnetic structures of FeGe. Yellow and purple spheres represent Fe and Ge atoms, respectively, while arrows denote magnetic moments of Fe atoms. (a) Top view of FeGe. The exchange interactions J_i denote the ith-nearest-neighbor interactions between Fe ions within kagome layers. (b) The exchange interactions J_{ci} denote the ith-nearest-neighbor interactions between Fe ions on the nearest kagome layers. (c) The exchange interactions $J_{c'i}$ denote the ith-nearest-neighbor interactions between Fe ions on the next-nearest kagome layers.

−50 meV) [7–10]. Note that the distance in J_1 is 2.5 Å while the others are all greater than 4 Å. Though there are also AFM in-plane magnetic interactions such as in-plane next-nearest-neighbor coupling J_2, they are at least an order of magnitude smaller than J_1, resulting in each FM kagome layer. As the out-of-plane nearest-neighbor coupling, J_{c1} is estimated to be 8.44 meV. It makes the magnetic moments stacked antiferromagnetically between kagome layers, consequently resulting in the A-type AFM order in kagome FeGe, which is consistent with the experiment [51]. It is worth mentioning that SOC always exists and leads to the DM interactions even in the centrosymmetric compound FeGe, since not all Fe-Fe bonds

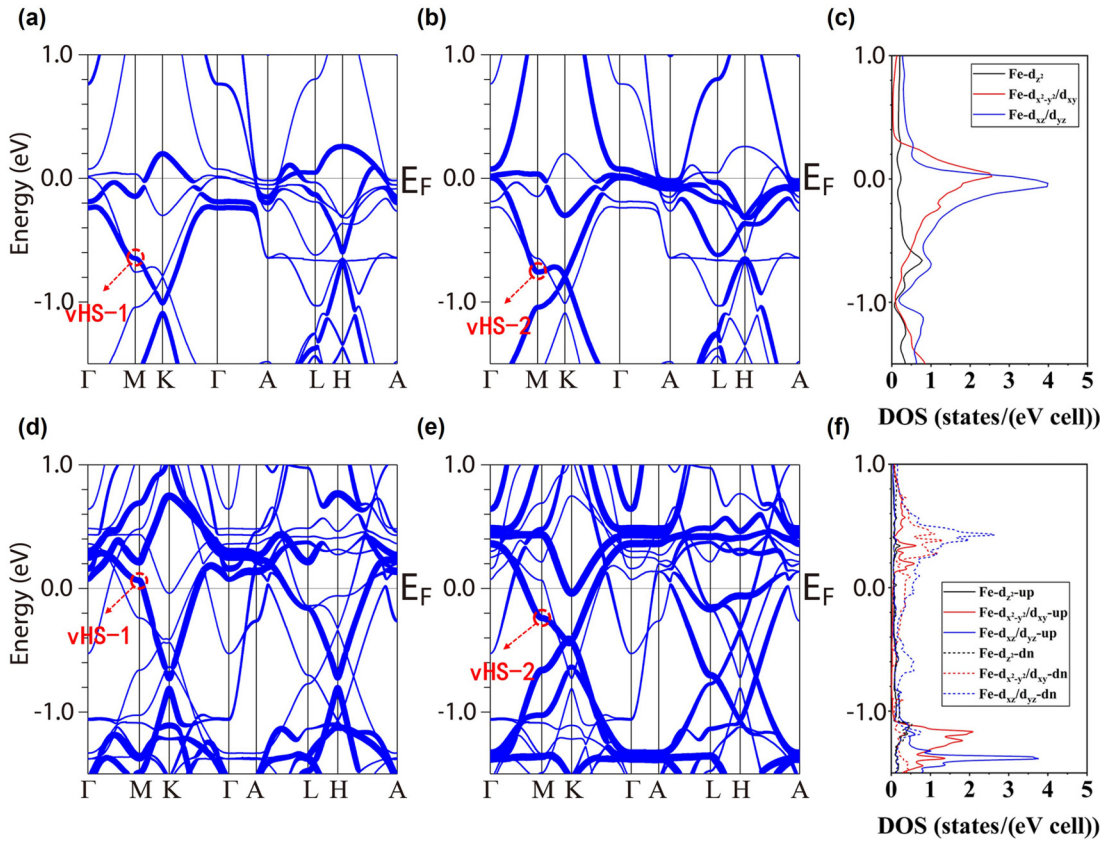

FIG. 2. (a), (b) Orbital-resolved band structure of Fe-$d_{xy}/d_{x^2-y^2}$ and Fe-d_{xz}/d_{yz} for nonmagnetic FeGe from LDA + SOC calculation. (c) Partial density of states of Fe atom located at (1/2,0,0) for nonmagnetic FeGe from LDA + SOC calculation. (d), (e) Orbital-resolved band structure of Fe-$d_{xy}/d_{x^2-y^2}$ and Fe-d_{xz}/d_{yz} for A-type AFM configuration with spin orientations along the (001) direction from LSDA + SOC calculation. (f) Partial density of states of Fe atom located at (1/2,0,0) for A-type AFM configuration from LSDA + SOC calculation.

have inversion symmetry. For the equivalent DM interactions connected by the crystal symmetry (see Tables VIII–X in the Appendix), we only present one of them as a representative. As shown in Table I, the in-plane nearest-neighbor $\mathbf{D}_1$ has the form of $(0, 0, D_1^z)$ according to the crystal symmetry and D_1^z is estimated to be 0.03 meV. Meanwhile, the in-plane next-nearest neighbor $\mathbf{D}_2$ is estimated to be $(0, 0, -0.12)$ meV. For the out-of-plane nearest neighbor, $\mathbf{D}_{c1}$ is zero because its bond has an inversion center. The other calculated DM interactions are also listed in Table I, and most of them are small in the order of 0.01 meV.

To explore the magnetic anisotropy in kagome FeGe, we consider the MAE with the expression $E_{\mathrm{MAE}} = K_2 \sin^2\theta + K_4 \sin^4\theta$ [51,54–56], neglecting terms of order higher than four, where θ is the angle between the magnetic moment and the z axis. The values of K_2 and K_4 are estimated to be 0.066 meV and 0.018 meV, respectively, based on the approach of Refs. [64,65], which are in reasonable agreement with the experimental values 0.021 meV [56] and 0.012 meV [51]. Here K_2 and K_4 are both positive, making out-of-plane magnetization favored, which is different from the easy-plane anisotropy in FeSn [8]. Note that positive K_4 is the requirement for the stability of the double cone magnetic structure, which will be discussed below.

Based on the calculated spin exchange parameters, we calculate Curie-Weiss temperature and Néel temperature by fitting the relationship curve between the inverse of the magnetic susceptibility and temperature from MC simulations [82–84]. The θ_{CW} and T_N are calculated to be -219 K and 370 K, respectively, which agree well with the experimental results ($\theta_{\mathrm{CW}} = -200$ K, $T_N = 410$ K) [51]. This implies that our calculated results of magnetic interactions are reliable. The relative low value of the frustration index $|\theta_{\mathrm{CW}}|/T_N$ (smaller than 1) reveals the interplay of the FM and AFM interactions [86], which is also verified by our calculated results of spin exchange couplings in Table I.

Similar to the electronic structure of a kagome lattice, the spin wave for a localized spin model with FM nearest-neighbor magnetic exchange also yields a flat magnetic band and a Dirac magnon [87]. Using the calculated spin model parameters, one can obtain the magnon spectrum [88,89]. The calculated spin-wave dispersion along the high-symmetry axis is shown in Fig. 3, which basically captures the key features of kagome lattice geometry. Similar to the FeSn case [7–10] (see Appendix), strongly dispersive magnons in the xy plane extend to about 260 meV, where the magnon dispersion along the out-of-plane direction has a relatively small bandwidth of less than 15 meV, reflecting the quasi-two-dimensional magnetic properties in kagome FeGe. Meanwhile, the Dirac-like node appears at the K point at about 107 meV, and we find that DM interactions introduce a gap around 1 meV at the Dirac point, as shown in the inset of Fig. 3. Furthermore, the single-ion anisotropy produces a spin gap of about 2 meV, which could be verified in future inelastic neutron scattering experiments.

B. The double cone magnetic structure

At $T_{\mathrm{canting}} = 60$ K, the kagome lattice FeGe becomes a c-axis double cone AFM structure [51,52,54–56], where the

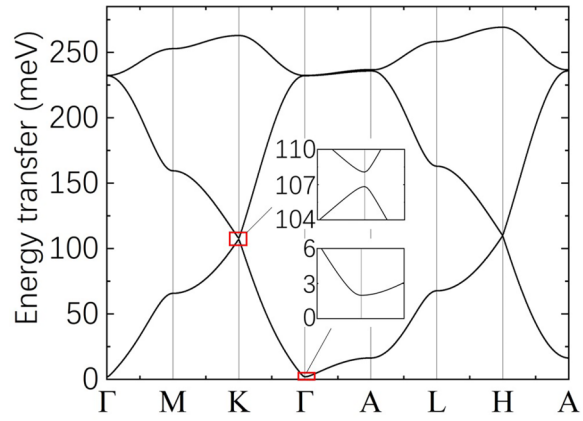

FIG. 3. Calculated spin-wave dispersion curves along the high-symmetry axis for FeGe. The insets show the spin gap at the Γ point induced by easy-axis anisotropy, and the gap located at about 107 meV of K point induced by DM interactions.

magnetic ground state could be written as Eq. (A6) in the Appendix. Considering the magnetic interactions and the MAE, the total energy of the double cone spin structure could be written as Eq. ((A8)) in the Appendix. When DM interactions are not considered, the extremum condition of the total energy gives the equilibrium value of wave vector δ and the cone half angle θ [i.e., Eqs. (A9) and (A10) in the Appendix]:

$$\cos\delta = \frac{\sum_i N_{ci} J_{ci}}{4\sum_i N_{c'i} J_{c'i}}, \tag{1}$$

$$\sin^2\theta = -\frac{K_2 - \frac{1}{2N}\sum_i N_{c'i} J_{c'i}\delta^4}{2K_4}. \tag{2}$$

Note that the minimum of the total energy requires that the second derivative of Eq. (A8) in the Appendix is positive, thus K_4 must be positive. Hence $K_2 - \frac{1}{2N}\sum_i N_{c'i} J_{c'i}\delta^4$ [i.e., the numerator of Eq. (2)] must be negative. However, our reasonable magnetic parameters cannot explain the double cone magnetic ground state. The value of wave vector δ is small in experimental measurement (0.17 in Ref. [51] and 0.25 in Ref. [53]), thus δ^4 is around 0.001. Meanwhile, the value of $\frac{1}{2N}\sum_i N_{c'i} J_{c'i}$ is of the order of 1 meV, which obviously cannot explain the double cone magnetic structure [51].

We thus consider the effect of DM interactions on double cone spin structure. Since the exchange interactions between two next-nearest-neighbor kagome layers are relatively small, we only consider the Heisenberg and DM interactions between two nearest neighbor kagome layers, i.e., J_{ci} and $\mathbf{D}_{ci}$. We find that wave vector δ and the cone half angle θ have the expressions as [i.e., Eqs. (A11) and (A12) in the Appendix]

$$\tan\delta = \frac{\sum_{i,j} D^z_{ci,j}}{\sum_i N_{ci} J_{ci}}, \tag{3}$$

$$\sin^2\theta = -\frac{K_2 - \frac{1}{2N}\sum_{i,j} D^z_{ci,j}\delta}{2K_4}. \tag{4}$$

It should be noted that, comparing Eqs. (2) and (4), DM interactions are much more efficient than Heisenberg interactions for causing double cone spin structures since δ is small. Though the space group $P6/mmm$ of the high-temperature phase in FeGe has a global inversion center, not all Fe-Fe

bonds have inversion symmetry and DM interactions could exist. However, according to the inversion symmetry of space group $P6/mmm$, the total contribution of DM interactions to the energy of the double cone magnetic structure in Eq. (A8) is absent, i.e., $\sum_{i,j} D^z_{ci,j} = 0$ (see Appendix). Meanwhile, mirror symmetries in space group $P6/mmm$ would also eliminate the contribution of DM interactions based on the symmetry analysis. Therefore, DM interactions have no net contribution to the double cone magnetic structure with the symmetry of high-temperature phase. For the CDW phases with the space group of $P6/mmm$ suggested by Refs. [48,49] (the first two structures of Table XI in the Appendix), the total contribution of DM interactions is still absent and cannot explain the magnetic ground state of double cone spin structure.

C. The interplay of CDW and double cone structure

As mentioned above, DM interactions play a more important role in the double cone spin structure. Meanwhile, it is very sensitive to atomic displacements. Therefore, in the following we explore the CDW phases with symmetry-allowed DM contribution to the double cone spin structure, which may explain the canted magnetic ground state.

The $2 \times 2 \times 2$ supercell structure of CDW phase (compared with the nonmagnetic pristine phase) is suggested experimentally [45,46,48,49]. Considering all CDW phases whose associated point group is in the maximal subgroups of D_{6h}, we find 68 different possible CDW phases which are the subgroups of the parent $P6/mmm$ phase with $2 \times 2 \times 2$ supercell (see details in the Appendix). The corresponding relations of atomic positions between the pristine phase and these proposed CDW phases are all summarized in Tables XI–XV of the Appendix.

Note that the inversion symmetry and mirror symmetries would all eliminate the net contribution of DM interactions as discussed above. We find that among these 68 proposed CDW phases, only four distorted structures break all these symmetries above, and can lead to nonzero DM contribution in Eq. (A8) of the Appendix. We list the corresponding Wyckoff positions (WPs) and the coordinates of the atoms in the pristine phase and these four CDW phases in Table II. They comes from two space groups $P622$ and $P6_322$. It should be mentioned that there are two different CDW phases for each of these two space groups, which are labeled as types I and II in Table II. The CDW phase with $P622$ space group is also suggested in Ref. [45]. The single crystals have $Fe_{1.00}Ge_{0.98}$ stoichiometry reported by Ref. [45], and the influence of these defects on the formation of the crystal CDW phase and magnetic structure needs further research.

Raman spectroscopy is a fast and usually nondestructive technique which can be used to characterize the structural distortion of materials. Based on the atomic coordinates in Table II, we predict the irreducible representation of the Raman active modes of these four proposed CDW phases using symmetry analysis [90]. For $P622$ type-I and type-II CDW phases, the Raman active modes are $8A_1 + 26E_1 + 22E_2$ and $10A_1 + 26E_1 + 22E_2$. Meanwhile, for $P6_322$ types I and II, the Raman active modes are $8A_1 + 24E_1 + 24E_2$ and $10A_1 + 24E_1 + 24E_2$, respectively. Note that even within the same symmetry of space group $P622$, the different structural distortion of CDW phases $P622$ types I and II could result in the different number of Raman active modes (56 and 58, respectively), which could be identified by Raman spectroscopy.

IV. CONCLUSION

In conclusion, we systematically analyze the electronic and magnetic properties of kagome FeGe. Our numerical results show that this material is a magnetic metal exhibiting large magnetic splitting around 1.8 eV. The magnetic splitting makes the flat bands away from the Fermi level and brings two vHSs near the Fermi level. We estimate the magnetic parameters and find that the FM nearest-neighbor J_1 dominates over the others, while the magnetic interactions between nearest kagome layers favors AFM. Based on these spin exchange parameters, the calculated Néel temperature and Curie-Weiss temperature also agree well with the experiments. Furthermore, the magnetic excitation spectra are calculated using linear spin wave theory and a spin gap about 2 meV is predicted. Note that the double cone magnetic transition at a lower temperature cannot be reproduced by these reasonable magnetic parameters. Meanwhile, due to the inversion symmetry and mirror symmetries in the space group $P6/mmm$ of the high-temperature phase, the total contribution of DM interactions to the double cone magnetic structure is absent. Since DM interactions are very sensitive to small atomic displacements and symmetry restrictions, and also much more efficient than Heisenberg interactions for causing this canted spin structure, we propose that the double cone spin structure may arise from the structural distortion. We explore 68 possible CDW phases of kagome FeGe which are subgroups of the pristine phase with $2 \times 2 \times 2$ supercell, and four symmetry-allowed CDW structures which have nonzero DM contribution and may result in double cone spin structure are proposed. These four CDW phases belong to two space groups $P622$ and $P6_322$, and we further propose that they can be identified from their different numbers of Raman active peaks. Therefore, we believe that symmetry analysis plays an important role in exploring the possible structural distortion in complex magnetic configurations.

ACKNOWLEDGMENTS

This work was supported by the NSFC (No. 12188101, 11834006, 12004170), National Key R&D Program of China (No. 2022YFA1403601), Natural Science Foundation of Jiangsu Province, China (Grant No. BK20200326), the excellent programme in Nanjing University, and Innovation

TABLE III. The calculated total energies (Ry) of FeGe and magnetic moments of Fe ions (μ_B) with different k-point meshes from LSDA+SOC calculations.

k mesh	Total energy (Ry)	Magnetic moment (μ_B)
$(4 \times 4 \times 2)$	−40462.67056	1.46732
$(5 \times 5 \times 3)$	−40462.67243	1.56920
$(7 \times 7 \times 3)$	−40462.67267	1.56931
$(8 \times 8 \times 4)$	−40462.67118	1.55428
$(13 \times 13 \times 7)$	−40462.67112	1.55122

TABLE IV. The calculated Heisenberg interactions (meV) with different k-point meshes of FeGe from LSDA+SOC calculations, respectively.

k mesh	(4 × 4 × 2)	(5 × 5 × 3)	(7 × 7 × 3)	(8 × 8 × 4)	(13 × 13 × 7)
J_1	−39.91	−43.08	−43.21	−42.11	−41.97
J_2	4.26	5.31	5.35	5.37	5.49
J_{c1}	7.43	8.00	8.05	7.96	8.44
J_{c2}	−2.32	−2.19	−2.16	−2.17	−2.04
J_{c3}	1.69	1.91	1.89	1.94	1.81
$J_{c'1}$	1.91	−1.41	−1.41	−0.40	−0.66
$J_{c'2}$	−0.70	0.26	0.24	0.09	0.09

Program for Quantum Science and Technology (No. 2021ZD0301902). X.W. also acknowledges the support from the Tencent Foundation through the XPLORER PRIZE.

APPENDIX

1. The k-point mesh convergence test

To validate the reliability of k-point mesh convergence, we perform first-principles calculations with different k-point meshes from LSDA + SOC calculations. The calculated total energies and magnetic moments of the Fe ions are presented in Table III. We also supplement the calculated Heisenberg and DM interactions with different k-point meshes in Tables IV and V. We believe that a 13 × 13 × 7 k-mesh can provide a relatively accurate description of the properties of the material.

2. Band structures from different exchange-correlation potentials

We perform the first-principles calculations using different exchange-correlation potentials including standard PBE-GGA [91], LSDA [92], WC-GGA [93], and PBEsol-GGA [94]. The band structures from different exchange-correlation functionals are shown in Fig. 4, which are almost the same.

3. The convergence test for cell size in MC simulation

The convergence test for the number of unit cells in MC simulation are shown in Table VI. The calculated Néel temperature and Curie-Weiss temperature exhibit little variation with varying unit cell numbers. Therefore, we believe that the calculated results obtained with the current cell size are reliable.

4. The density of states in kagome FeGe

The partial density of states (DOS) of FeGe from LSDA + SOC calculations are shown in Fig. 5.

5. The calculated magnetic moments for different values of U

The calculated magnetic moments of Fe ions from the LSDA + SOC + U(= 0, 1, 2, 3, and 4 eV) calculations are summarized in Table VII. It can be seen that the calculated magnetic moment with $U = 0$ is in the best agreement with the experimental results (1.7 μ_B) [52,55]. Therefore, we believe that the LSDA + SOC calculation could present a reliable description of the magnetic properties of kagome FeGe.

6. Spin-wave dispersion curves of FeSn

The calculated spin-wave dispersion of FeSn along the high-symmetry axis is shown in Fig. 6 according to the results of magnetic interactions in Ref. [9]. The spin excitation spectrum in FeSn with strong dispersion in the kagome plane extend beyond 330 meV. Conversely, the magnon dispersion along the out-of-plane direction has a bandwidth of less than 20 meV, indicating the dominant magnetic interactions are within the kagome-lattice planes. Moreover, the spin-wave dispersion presents a sharp linear magnon band crossing at around 120 meV at the K point. The high-energy spectra in FeSn have a larger bandwidth compared to that in FeGe, which may be attributed to the greater J_2 value in FeSn.

7. The symmetry restrictions on the magnetic interactions

Here we consider a general pairwise spin model

$$H = \sum_{l,n,l',n'} \mathbf{S}_{ln} \mathbf{J}_{\mathbf{R}_l+\boldsymbol{\tau}_n,\mathbf{R}_{l'}+\boldsymbol{\tau}_{n'}} \mathbf{S}_{l'n'}, \tag{A1}$$

TABLE V. The calculated DM interactions (meV) with different k-point meshes of FeGe from LSDA+SOC calculations, respectively.

k-mesh	(4 × 4 × 2)	(5 × 5 × 3)	(7 × 7 × 3)	(8 × 8 × 4)	(13 × 13 × 7)
$\mathbf{D}_1$	(0.00, 0.00, 0.08)	(0.00, 0.00, 0.02)	(0.00, 0.00, 0.02)	(0.00, 0.00, 0.02)	(0.00, 0.00, 0.03)
$\mathbf{D}_2$	(0.00, 0.00, −0.08)	(0.00, 0.00, −0.14)	(0.00, 0.00, −0.14)	(0.00, 0.00, −0.09)	(0.00, 0.00, −0.12)
$\mathbf{D}_{c1}$	(0.00, 0.00, 0.00)	(0.00, 0.00, 0.00)	(0.00, 0.00, 0.00)	(0.00, 0.00, 0.00)	(0.00, 0.00, 0.00)
$\mathbf{D}_{c2}$	(0.14, −0.17, −0.10)	(0.02, −0.02, −0.15)	(0.02, −0.03, −0.15)	(0.05, −0.05, −0.08)	(0.01, −0.02, −0.07)
$\mathbf{D}_{c3}$	(0.02, −0.23, 0.00)	(0.04, −0.02, −0.03)	(0.06, −0.03, 0.02)	(0.10, −0.10, −0.07)	(0.07, −0.04, −0.09)
$\mathbf{D}_{c'1}$	(0.00, 0.00, 0.00)	(0.00, 0.00, 0.00)	(0.00, 0.00, 0.00)	(0.00, 0.00, 0.00)	(0.00, 0.00, 0.00)
$\mathbf{D}_{c'2}$	(−0.41, −0.20, 0.00)	(−0.08, −0.16, −0.04)	(−0.05, −0.12, −0.04)	(−0.08, −0.08, −0.02)	(−0.04, −0.09, −0.03)

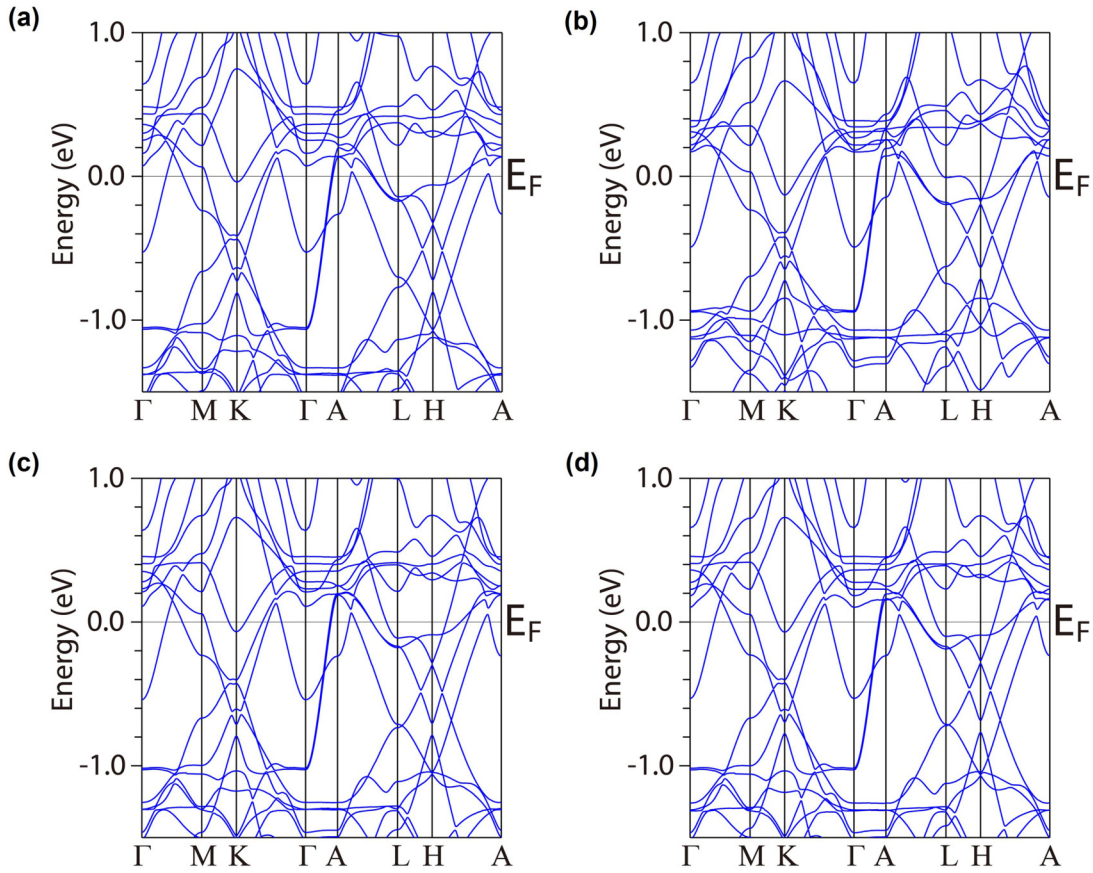

FIG. 4. The band structures for A-type AFM configuration of FeGe from different exchange-correlation potentials, (a) standard PBE-GGA [91], (b) LSDA [92], (c) WC-GGA [93], (d) PBEsol-GGA [94].

where $\mathbf{J}_{\mathbf{R}_l+\boldsymbol{\tau}_n,\mathbf{R}_{l'}+\boldsymbol{\tau}_{n'}}$, a 3×3 tensor, represents the spin exchange parameters. $\mathbf{R}_l$ and $\boldsymbol{\tau}_n$ represent the lattice translation vector and the position of magnetic ions in the lattice basis, and $\mathbf{S}_{ln}$ means the spin at the site of $\mathbf{R}_l+\boldsymbol{\tau}_n$.Translation symmetry will restrict $\mathbf{J}_{\mathbf{R}_l+\boldsymbol{\tau}_n,\mathbf{R}_{l'}+\boldsymbol{\tau}_{n'}}$ to be only related to $\mathbf{J}_{\boldsymbol{\tau}_n,\boldsymbol{\tau}_{n'}+\mathbf{R}_{l''}}$, where $R_{l''}=R_{l'}-R_l$, irrespective of the starting unit cell. Other spatial symmetries will also give restrictions on the magnetic exchange interactions. We consider a general space group element $\{\alpha|\mathbf{t}\}$, where the left part represents the rotation and the right part means the lattice translation. Supposing under this symmetry operator, $\mathbf{R}_m+\boldsymbol{\tau}_p$ and $\mathbf{R}_{m'}+\boldsymbol{\tau}_{p'}$ transfer to $\mathbf{R}_l+\boldsymbol{\tau}_n$ and $\mathbf{R}_{l'}+\boldsymbol{\tau}_{n'}$, respectively, meanwhile the transformation of spin becomes $\mathbf{S}_{mp}=M(\alpha)\mathbf{S}_{ln}$, where $M(\alpha)$ is the representation matrix of the proper rotation part of the operation α in the coordinate system, we get the following expression:

$$\begin{aligned} H &= \sum_{l,n,l',n'} \mathbf{S}_{ln}\mathbf{J}_{\mathbf{R}_l+\boldsymbol{\tau}_n,\mathbf{R}_{l'}+\boldsymbol{\tau}_{n'}}\mathbf{S}_{l'n'} \\ &= \sum_{l,n,l',n'} \mathbf{S}_{ln}M^{\dagger}(\alpha)M(\alpha)\mathbf{J}_{\mathbf{R}_l+\boldsymbol{\tau}_n,\mathbf{R}_{l'}+\boldsymbol{\tau}_{n'}}M^{\dagger}(\alpha)M(\alpha)\mathbf{S}_{l'n'} \\ &= \sum_{m,p,m',p'} \mathbf{S}_{mp}[M(\alpha)\mathbf{J}_{\mathbf{R}_l+\boldsymbol{\tau}_n,\mathbf{R}_{l'}+\boldsymbol{\tau}_{n'}}M^{\dagger}(\alpha)]\mathbf{S}_{m'p'}. \end{aligned} \tag{A2}$$

Then the exchange interactions should satisfy the following condition:

$$\mathbf{J}_{\mathbf{R}_m+\boldsymbol{\tau}_p,\mathbf{R}_{m'}+\boldsymbol{\tau}_{p'}} = M(\alpha)\mathbf{J}_{\mathbf{R}_l+\boldsymbol{\tau}_n,\mathbf{R}_{l'}+\boldsymbol{\tau}_{n'}}M^{\dagger}(\alpha). \tag{A3}$$

After decomposing the 3×3 tensor $\mathbf{J}$ into scalar Heisenberg term J and the vector DM term $\mathbf{D}$ as in the main text, we

TABLE VI. The calculated T_N and θ_{CW} (K) of FeGe from MC simulation with different unit cell numbers with periodic boundary conditions.

Unit cells	T_N	θ_{CW}
$(6\times6\times6)$	371	−222
$(8\times8\times8)$	368	−216
$(10\times10\times10)$	368	−219
$(16\times16\times16)$	370	−219

TABLE VII. The calculated magnetic moments of Fe ions evaluated from LSDA + SOC (+ U) calculations with different values of U.

U (eV)	Moment (μ_B)
0.0	1.551
1.0	2.066
2.0	2.406
3.0	2.620
4.0	2.772

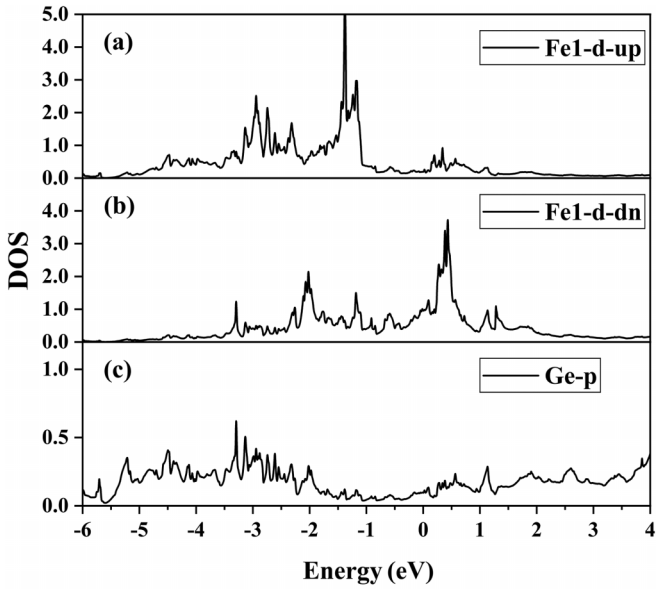

FIG. 5. Partial DOS of FeGe from LSDA + SOC calculations. The Fermi energy is set to zero. (a) and (b) represent the spin-up and spin-down channel of d orbitals in Fe1 atom located at (1/2,0,0), while (c) represents the DOS of Ge-p orbitals.

obtain the following results:

$$J_{\mathbf{R}_m+\boldsymbol{\tau}_p,\mathbf{R}_{m'}+\boldsymbol{\tau}_{p'}} = J_{\mathbf{R}_l+\boldsymbol{\tau}_n,\mathbf{R}_{l'}+\boldsymbol{\tau}_{n'}},$$
$$\mathbf{D}_{\mathbf{R}_m+\boldsymbol{\tau}_p,\mathbf{R}_{m'}+\boldsymbol{\tau}_{p'}} = M(\alpha)\mathbf{D}_{\mathbf{R}_l+\boldsymbol{\tau}_n,\mathbf{R}_{l'}+\boldsymbol{\tau}_{n'}}. \quad \text{(A4)}$$

Meanwhile, it is should be noted that the Heisenberg and DM interactions obey the following commutation relations:

$$J_{\mathbf{R}_{l'}+\boldsymbol{\tau}_{n'},\mathbf{R}_l+\boldsymbol{\tau}_n} = J_{\mathbf{R}_l+\boldsymbol{\tau}_n,\mathbf{R}_{l'}+\boldsymbol{\tau}_{n'}},$$
$$\mathbf{D}_{\mathbf{R}_{l'}+\boldsymbol{\tau}_{n'},\mathbf{R}_l+\boldsymbol{\tau}_n} = -\mathbf{D}_{\mathbf{R}_l+\boldsymbol{\tau}_n,\mathbf{R}_{l'}+\boldsymbol{\tau}_{n'}}. \quad \text{(A5)}$$

According to the above equations [i.e., Eqs. (A4) and (A5)], one can obtain the symmetry-restricted magnetic interactions for kagome FeGe with space group $P6/mmm$, as shown in Table VIII–X. Note that the equivalent $\mathbf{D}_i$'s are labeled as the subindex of j, i.e., $\mathbf{D}_{i,j}$ in Table VIII–X.

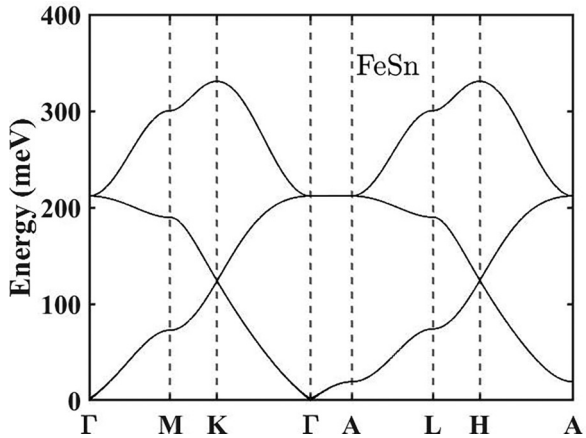

FIG. 6. Calculated spin-wave dispersion curves along the high-symmetry axis for FeSn.

TABLE VIII. The distances, the bond information, and the symmetry-restricted interactions of corresponding Fe ions within xy planes. Here n, n', and R_l correspond to $\mathbf{J}_{\tau_n,\tau_{n'}+\mathbf{R}_l}$, where R_l and τ_n represent the lattice translation vector and the position of magnetic ions in the lattice basis. Three magnetic ions are located at τ_1 (1/2, 0, 0), τ_2 (0, 1/2, 0), and τ_3 (1/2, 1/2, 0). The equivalent $\mathbf{D}_i$'s are labeled as the subindex of j, i.e., $\mathbf{D}_{i,j}$ in the table.

Distance (Å)	n	n'	R_l	J	DM
2.50	3	1	(0,1,0)	J_1	$\mathbf{D}_{1,1}(0,0,D_1^z)$
	1	2	(0,–1,0)	J_1	$\mathbf{D}_{1,2}(0,0,D_1^z)$
	2	3	(0,0,0)	J_1	$\mathbf{D}_{1,3}(0,0,D_1^z)$
	3	1	(0,0,0)	J_1	$\mathbf{D}_{1,4}(0,0,D_1^z)$
	1	2	(1,0,0)	J_1	$\mathbf{D}_{1,5}(0,0,D_1^z)$
	2	3	(−1,0,0)	J_1	$\mathbf{D}_{1,6}(0,0,D_1^z)$
4.33	1	2	(1,–1,0)	J_2	$\mathbf{D}_{2,1}(0,0,D_2^z)$
	2	3	(0,1,0)	J_2	$\mathbf{D}_{2,2}(0,0,D_2^z)$
	3	1	(−1,0,0)	J_2	$\mathbf{D}_{2,3}(0,0,D_2^z)$
	1	2	(0,0,0)	J_2	$\mathbf{D}_{2,4}(0,0,D_2^z)$
	2	3	(−1,–1,0)	J_2	$\mathbf{D}_{2,5}(0,0,D_2^z)$
	3	1	(1,1,0)	J_2	$\mathbf{D}_{2,6}(0,0,D_2^z)$

8. The details of double cone structure

According to the experimental works [51,54–56], in hexagonal FeGe there is a transition from a uniaxial spin system to a double cone spin structure at $T_{\text{canting}} = 60$ K [51], which is expressed by the following equations:

$$\langle S^x\rangle = S\sin\theta\cos\left((\pi\pm\delta)\frac{z}{c}+\varphi\right),$$
$$\langle S^y\rangle = S\sin\theta\sin\left((\pi\pm\delta)\frac{z}{c}+\varphi\right),$$
$$\langle S^z\rangle = S\cos\theta\cos\left(\frac{\pi z}{c}\right), \quad \text{(A6)}$$

where θ is the cone half angle and c represents the lattice parameter. If $\delta = 0$, there will be a simple tilting of the spins. When δ represents the small angle, Eq. (A6) gives a double cone spin structure. Following previous works [51,54–56], here we consider the MAE with the expression neglecting terms of order higher than four written as

$$E_{\text{MAE}} = K_2\sin^2\theta + K_4\sin^4\theta. \quad \text{(A7)}$$

Therefore, the total energy of Eqs. (A1) and (A7) in double cone spin structure per unit cell could be written as

$$\begin{aligned}E(\delta,\theta) = &\sum_i N_{ci}J_{ci}(-\sin^2\theta\cos\delta-\cos^2\theta)\\ &+\sum_i N_{c'i}J_{c'i}(\sin^2\theta\cos 2\delta+\cos^2\theta)\\ &-\sum_{i,j}D^z_{ci,j}(\sin^2\theta\sin\delta)\\ &-\sum_{i,j}D^z_{c'i,j}(\sin^2\theta\sin 2\delta)\\ &+N(K_2\sin^2\theta+K_4\sin^4\theta), \quad \text{(A8)}\end{aligned}$$

TABLE IX. The distances, the bond information, and the symmetry-restricted interactions of corresponding Fe ions between nearest-neighbor (001) planes. Here n, n', and R_l correspond to $\mathbf{J}_{\tau_n,\tau_{n'}+\mathbf{R}_l}$, where R_l and τ_n represent the lattice translation vector and the position of magnetic ions in the lattice basis. Three magnetic ions are located at τ_1 (1/2, 0, 0), τ_2 (0, 1/2, 0), and τ_3 (1/2, 1/2, 0). The equivalent $\mathbf{D}_{ci}$'s are labeled as the subindex of j, i.e., $\mathbf{D}_{ci,j}$ in the table.

Distance (Å)	n	n'	R_l	J	DM
4.05	1	1	(0,0,1)	J_{c1}	$\mathbf{D}_{c1,1}(0,0,0)$
	2	2	(0,0,1)	J_{c1}	$\mathbf{D}_{c1,2}(0,0,0)$
	3	3	(0,0,1)	J_{c1}	$\mathbf{D}_{c1,3}(0,0,0)$
4.76	3	1	(0,0,1)	J_{c2}	$\mathbf{D}_{c2,1}(D^x_{c2}, -\sqrt{3}D^x_{c2}, D^z_{c2})$
	1	2	(1,0,1)	J_{c2}	$\mathbf{D}_{c2,2}(D^x_{c2}, \sqrt{3}D^x_{c2}, D^z_{c2})$
	2	3	(−1,0,1)	J_{c2}	$\mathbf{D}_{c2,3}(-2D^x_{c2}, 0, D^z_{c2})$
	3	1	(0,1,1)	J_{c2}	$\mathbf{D}_{c2,4}(-D^x_{c2}, \sqrt{3}D^x_{c2}, D^z_{c2})$
	1	2	(0,−1,1)	J_{c2}	$\mathbf{D}_{c2,5}(-D^x_{c2}, -\sqrt{3}D^x_{c2}, D^z_{c2})$
	2	3	(0,0,1)	J_{c2}	$\mathbf{D}_{c2,6}(2D^x_{c2}, 0, D^z_{c2})$
	1	3	(0,−1,1)	J_{c2}	$\mathbf{D}_{c2,7}(-D^x_{c2}, \sqrt{3}D^x_{c2}, -D^z_{c2})$
	2	1	(0,1,1)	J_{c2}	$\mathbf{D}_{c2,8}(-D^x_{c2}, -\sqrt{3}D^x_{c2}, -D^z_{c2})$
	3	2	(0,0,1)	J_{c2}	$\mathbf{D}_{c2,9}(2D^x_{c2}, 0, -D^z_{c2})$
	1	3	(0,0,1)	J_{c2}	$\mathbf{D}_{c2,10}(D^x_{c2}, -\sqrt{3}D^x_{c2}, -D^z_{c2})$
	2	1	(−1,0,1)	J_{c2}	$\mathbf{D}_{c2,11}(D^x_{c2}, \sqrt{3}D^x_{c2}, -D^z_{c2})$
	3	2	(1,0,1)	J_{c2}	$\mathbf{D}_{c2,12}(-2D^x_{c2}, 0, -D^z_{c2})$
5.93	2	1	(−1,1,1)	J_{c3}	$\mathbf{D}_{c3,1}(-\sqrt{3}D^y_{c3}, D^y_{c3}, -D^z_{c3})$
	3	2	(0,−1,1)	J_{c3}	$\mathbf{D}_{c3,2}(0, -2D^y_{c3}, -D^z_{c3})$
	1	3	(1,0,1)	J_{c3}	$\mathbf{D}_{c3,3}(\sqrt{3}D^y_{c3}, D^y_{c3}, -D^z_{c3})$
	2	1	(0,0,1)	J_{c3}	$\mathbf{D}_{c3,4}(\sqrt{3}D^y_{c3}, -D^y_{c3}, -D^z_{c3})$
	3	2	(1,1,1)	J_{c3}	$\mathbf{D}_{c3,5}(0, 2D^y_{c3}, -D^z_{c3})$
	1	3	(−1,−1,1)	J_{c3}	$\mathbf{D}_{c3,6}(-\sqrt{3}D^y_{c3}, -D^y_{c3}, -D^z_{c3})$
	1	2	(0,0,1)	J_{c3}	$\mathbf{D}_{c3,7}(\sqrt{3}D^y_{c3}, -D^y_{c3}, D^z_{c3})$
	2	3	(−1,−1,1)	J_{c3}	$\mathbf{D}_{c3,8}(0, 2D^y_{c3}, D^z_{c3})$
	3	1	(1,1,1)	J_{c3}	$\mathbf{D}_{c3,9}(-\sqrt{3}D^y_{c3}, -D^y_{c3}, D^z_{c3})$
	1	2	(1,−1,1)	J_{c3}	$\mathbf{D}_{c3,10}(-\sqrt{3}D^y_{c3}, D^y_{c3}, D^z_{c3})$
	2	3	(0,1,1)	J_{c3}	$\mathbf{D}_{c3,11}(0, -2D^y_{c3}, D^z_{c3})$
	3	1	(−1,0,1)	J_{c3}	$\mathbf{D}_{c3,12}(\sqrt{3}D^y_{c3}, D^y_{c3}, D^z_{c3})$

TABLE X. The distances, bond information, and the symmetry-restricted interactions of corresponding Fe ions between next-nearest-neighbor (001) planes. Here n, n', and R_l correspond to $\mathbf{J}_{\tau_n,\tau_{n'}+\mathbf{R}_l}$, where R_l and τ_n represent the lattice translation vector and the position of magnetic ions in the lattice basis. Three magnetic ions are located at τ_1 (1/2, 0, 0), τ_2 (0, 1/2, 0), and τ_3 (1/2, 1/2, 0). The equivalent $\mathbf{D}_{c'i}$'s are labeled as the subindex of j, i.e., $\mathbf{D}_{c'i,j}$ in the table.

Distance (Å)	n	n'	R_l	J	DM
8.11	1	1	(0,0,2)	$J_{c'1}$	$\mathbf{D}_{c'1,1}(0,0,0)$
	2	2	(0,0,2)	$J_{c'1}$	$\mathbf{D}_{c'1,2}(0,0,0)$
	3	3	(0,0,2)	$J_{c'1}$	$\mathbf{D}_{c'1,3}(0,0,0)$
8.49	2	1	(0,1,2)	$J_{c'2}$	$\mathbf{D}_{c'2,1}(D^x_{c'2}, \sqrt{3}D^x_{c'2}, D^z_{c'2})$
	3	2	(0,0,2)	$J_{c'2}$	$\mathbf{D}_{c'2,2}(-2D^x_{c'2}, 0, D^z_{c'2})$
	1	3	(0,−1,2)	$J_{c'2}$	$\mathbf{D}_{c'2,3}(D^x_{c'2}, -\sqrt{3}D^x_{c'2}, D^z_{c'2})$
	2	1	(−1,0,2)	$J_{c'2}$	$\mathbf{D}_{c'2,4}(-D^x_{c'2}, -\sqrt{3}D^x_{c'2}, D^z_{c'2})$
	3	2	(1,0,2)	$J_{c'2}$	$\mathbf{D}_{c'2,5}(2D^x_{c'2}, 0, D^z_{c'2})$
	1	3	(0,0,2)	$J_{c'2}$	$\mathbf{D}_{c'2,6}(-D^x_{c'2}, \sqrt{3}D^x_{c'2}, D^z_{c'2})$
	1	2	(1,0,2)	$J_{c'2}$	$\mathbf{D}_{c'2,7}(-D^x_{c'2}, -\sqrt{3}D^x_{c'2}, -D^z_{c'2})$
	2	3	(−1,0,2)	$J_{c'2}$	$\mathbf{D}_{c'2,8}(2D^x_{c'2}, 0, -D^z_{c'2})$
	3	1	(0,0,2)	$J_{c'2}$	$\mathbf{D}_{c'2,9}(-D^x_{c'2}, \sqrt{3}D^x_{c'2}, -D^z_{c'2})$
	1	2	(0,−1,2)	$J_{c'2}$	$\mathbf{D}_{c'2,10}(D^x_{c'2}, \sqrt{3}D^x_{c'2}, -D^z_{c'2})$
	2	3	(0,0,2)	$J_{c'2}$	$\mathbf{D}_{c'2,11}(-2D^x_{c'2}, 0, -D^z_{c'2})$
	3	1	(0,1,2)	$J_{c'2}$	$\mathbf{D}_{c'2,12}(D^x_{c'2}, -\sqrt{3}D^x_{c'2}, -D^z_{c'2})$

where N_{ci} and $N_{c'i}$ are the corresponding number of neighbors of J_{ci} and $J_{c'i}$, and N represents the number of magnetic ions in one unit cell. When DM interactions are not considered, the extremum condition in total energy gives the equilibrium value of wave vector δ with the following equation [51,56]:

$$\cos\delta = \frac{\sum_i N_{ci}J_{ci}}{4\sum_i N_{c'i}J_{c'i}}, \tag{A9}$$

while the cone half angle θ has the expression

$$\sin^2\theta = -\frac{K_2 - \frac{1}{2N}\sum_i N_{c'i}J_{c'i}\delta^4}{2K_4}. \tag{A10}$$

A minimum in the total energy [see Eq. (A8)] will occur only if K_4 is positive, and Eq. (A10) requires that $K_2 - \frac{1}{2N}\sum_i N_{c'i}J_{c'i}\delta^4$ must be negative.

When the magnetic interactions including Heisenberg and DM interactions between two nearest-neighbor xy planes, i.e., J_{ci} and $\mathbf{D}_{ci}$, are considered, the equilibrium value of wave vector δ is obtained by the minimum in total energy written as

$$\tan\delta = \frac{\sum_{i,j} D^z_{ci,j}}{\sum_i N_{ci}J_{ci}}, \tag{A11}$$

where j is the subindex of the equivalent $\mathbf{D}_{ci}$'s. Meanwhile, we find the following expression for θ:

$$\sin^2\theta = -\frac{K_2 - \frac{1}{2N}\sum_{i,j} D^z_{ci,j}\delta}{2K_4} \tag{A12}$$

Note that in Eq. (A12), DM interactions are combined with only the first order of δ, and may be much more efficient than $J_{c'i}$ in Eq. (A10) since δ is small around 0.2 [51,53]. This implies that DM interactions may be the origin of double cone structure.

9. The symmetry analysis of CDW phases

The high-temperature phase FeGe crystallizes in space group $P6/mmm$, which has the generators $\{3^+_{001}|0\}$, $\{2_{001}|0\}$, $\{2_{110}|0\}$, and $\{-1|0\}$, where the left part represents the rotation and the right part means the lattice translation (here -1 denotes the inversion symmetry). According to the inversion symmetry, the total contribution of DM interactions to the energy of double cone magnetic structure in Eq. (A8) is absent, i.e., $\sum_{i,j} D^z_{ci,j} = 0$, which is easy to see from Tables IX and X. First, each kagome layer is still FM in the double cone magnetic state, thus the in-plane DM interactions are ineffective. For interlayer DM interactions with an inversion center such as $\mathbf{D}_{c1}$, the inversion symmetry restricts it to be zero, as shown in Table IX. Meanwhile, for other interlayer DM interactions, the inversion symmetry combines the equivalent DM

TABLE XI. The corresponding Wyckoff positions and the coordinates of the atoms in the pristine phase and CDW phases with different symmetries. (Part I.)

Pristine phase ($P6/mmm$)			SG191-$P6/mmm$ (type I)			SG191-$P6/mmm$ (type II)			SG194-$P6_3/mmc$ (type I)			SG194-$P6_3/mmc$(type II)		
	WP	Coordinates		WP	Coordinates		WP	Coordinates		WP	Coordinates		WP	Coordinates
Ge1	1*a*	(0, 0, 0)	Ge1	1*a*	(0, 0, 0)	Ge1	2*e*	(0, 0, *z*)	Ge1	2*a*	(0, 0, 0)	Ge1	2*b*	(0, 0, 1/4)
			Ge2	1*b*	(0, 0, 1/2)	Ge2	6*i*	(1/2, 0, *z*)	Ge2	6*g*	(1/2, 0, 0)	Ge2	6*h*	(*x*, 2x, 1/4)
			Ge3	3*f*	(1/2, 0, 0)									
			Ge4	3*g*	(1/2, 0, 1/2)									
Ge2	2*d*	(1/3, 2/3, 1/2)	Ge5	4*h*	(1/3, 2/3, *z*)	Ge3	2*c*	(1/3, 2/3, 0)	Ge3	2*c*	(1/3, 2/3, 1/4)	Ge3	4*f*	(1/3, 2/3, *z*)
			Ge6	12*o*	(*x*, 2x, *z*)	Ge4	2*d*	(1/3, 2/3, 1/2)	Ge4	2*d*	(1/3, 2/3, 1/4)	Ge4	12*k*	(*x*, 2x, *z*)
						Ge5	6*l*	(*x*, 2x, 0)	Ge5	6*h*	(*x*, 2x, 1/4)			
						Ge6	6*m*	(*x*, 2x, 1/2)	Ge6	6*h*	(*x*, 2x, 1/4)			
Fe	3*f*	(1/2, 0, 0)	Fe1	6*j*	(*x*, 0, 0)	Fe1	12*n*	(*x*, 2x, *z*)	Fe1	12*k*	(*x*, 0, 0)	Fe1	6*h*	(*x*, 2x, 1/4)
			Fe2	6*k*	(*x*, 0, 1/2)	Fe2	12*o*	(*x*, 0, *z*)	Fe2	12*k*	(*x*, 2x, *z*)	Fe2	6*h*	(*x*, 2x, 1/4)
			Fe3	6*l*	(*x*, 2x, 0)							Fe3	12*j*	(*x*, y, 1/4)
			Fe4	6*m*	(*x*, 2x, 1/2)									

Pristine phase ($P6/mmm$)			SG193-$P6_3/mcm$ (type I)			SG193-$P6_3/mcm$ (type II)			SG192-$P6/mcc$ (type I)			SG192-P6/mcc(type II)		
	WP	Coordinates		WP	Coordinates		WP	Coordinates		WP	Coordinates		WP	Coordinates
Ge1	1*a*	(0, 0, 0)	Ge1	2*b*	(0, 0, 0)	Ge1	2*a*	(0, 0, 1/4)	Ge1	2*b*	(0, 0, 0)	Ge1	2*b*	(0, 0, 1/4)
			Ge2	6*f*	(1/2, 0, 0)	Ge2	6*g*	(*x*, 0, 1/4)	Ge2	6*g*	(1/2, 0, 0)	Ge2	6*f*	(1/2, 0, 1/4)
Ge2	2*d*	(1/3, 2/3, 1/2)	Ge3	4*c*	(1/3, 2/3, 1/4)	Ge3	4*d*	(1/3, 2/3, 0)	Ge3	4*c*	(1/3, 2/3, 1/4)	Ge3	4*d*	(1/3, 2/3, *z*)
			Ge4	12*j*	(*x*, *y*, 1/4)	Ge4	12*i*	(*x*, 2x, 0)	Ge4	12*k*	(*x*, 2x, 1/4)	Ge4	12*l*	(*x*, y, 0)
Fe	3*f*	(1/2, 0, 0)	Fe1	12*i*	(*x*, 0, *z*)	Fe1	6*g*	(*x*, 0, 1/4)	Fe1	12*l*	(*x*, y, 0)	Fe1	12*j*	(*x*, 0, 1/4)
			Fe2	12*k*	(*x* 2x,0)	Fe2	6*g*	(*x*, 0, 1/4)	Fe2	12*l*	(*x*, y, 0)	Fe2	12*k*	(*x*, 2x, 1/4)
						Fe3	12*j*	(*x*, *y*, 1/4)						

Pristine phase ($P6/mmm$)			SG190-P$\bar{6}$2*c* (type I)			SG190-P$\bar{6}$2*c* (type II)			SG189-P$\bar{6}$ 2m (type I)			SG189-P $\bar{6}$2 m(type II)		
	WP	Coordinates		WP	Coordinates		WP	Coordinates		WP	Coordinates		WP	Coordinates
Ge1	1*a*	(0, 0, 0)	Ge1	2*a*	(0, 0, 0)	Ge1	2*b*	(0, 0, 1/4)	Ge1	1*a*	(0, 0, 0)	Ge1	2*e*	(0, 0, *z*)
			Ge2	6*g*	(*x*, 0, 0)	Ge2	6*h*	(*x*, *y*, 1/4)	Ge2	1*b*	(0, 0, 1/2)	Ge2	6i	(*x*, 0, *z*)
									Ge3	3*f*	(*x*, 0, 0)			
									Ge4	3g	(*x*, 0, 1/2)			
Ge2	2*d*	(1/3, 2/3, 1/2)	Ge3	2*c*	(1/3, 2/3, 1/4)	Ge3	4*f*	(1/3, 2/3, *z*)	Ge5	4*h*	(1/3, 2/3, *z*)	Ge3	2*c*	(1/3, 2/3, 0)
			Ge4	2*d*	(1/3, 2/3, 3/4)	Ge4	12*i*	(*x*, y, *z*)	Ge6	12*l*	(*x*, y, *z*)	Ge4	2*d*	(1/3, 2/3, 1/2)
			Ge5	6*h*	(*x*, y, 1/4)							Ge5	6*j*	(*x*, y, 0)
			Ge6	6*h*	(*x*, y, 1/4)							Ge6	6*k*	(*x*, y, 1/2)
Fe	3*f*	(1/2, 0, 0))	Fe1	6*g*	(*x*, 0, 0)	Fe1	6*h*	(*x*, y, 1/4)	Fe1	3*f*	(*x*, 0, 0)	Fe1	6i	(*x*, 0, *z*)
			Fe2	6*g*	(*x*, 0, 0)	Fe2	6*h*	(*x*, y, 1/4)	Fe2	3*f*	(*x*, 0, 0)	Fe2	6i	(*x*, 0, *z*)
			Fe3	12*i*	(*x*, y, *z*)	Fe3	6*h*	(*x*, y, 1/4)	Fe3	3g	(*x*, 0, 1/2)	Fe3	12*l*	(*x*, y, *z*)
						Fe4	6*h*	(*x*, y, 1/4)	Fe4	3g	(*x*, 0, 1/2)			
									Fe5	6*j*	(*x*, y, 0)			
									Fe6	6*k*	(*x*, y, 1/2)			

Pristine phase(P6/mmm)			SG188-P$\bar{6}$c2(type I)			SG188-P$\bar{6}$c2(type II)			SG187-P$\bar{6}$ m2(type I)			SG187-P $\bar{6}$m2(type II)		
	WP	Coordinates		WP	Coordinates		WP	Coordinates		WP	Coordinates		WP	Coordinates
Ge1	1*a*	(0, 0, 0)	Ge1	2*a*	(0, 0, 0)	Ge1	2*d*	(1/3, 2/3, 1/4)	Ge1	1*a*	(0, 0, 0)	Ge1	2h	(1/3, 2/3, *z*)
			Ge2	6*j*	(*x*, 2x, 0)	Ge2	6*k*	(*x*, y, 1/4)	Ge2	1*b*	(0, 0, 1/2)	Ge2	6n	(*x*, 2x, *z*)
									Ge3	3j	(*x*, 2x, 0)			
									Ge4	3k	(*x*, 2x, 1/2)			
Ge2	2*d*	(1/3, 2/3, 1/2)	Ge3	2*d*	(2/3, 1/3, 1/4)	Ge3	2*a*	(0, 0, 0)	Ge5	2i	(2/3, 1/3, *z*)	Ge3	1*a*	(0, 0, 0)
			Ge4	2f	(1/3, 2/3, 1/4)	Ge4	2*e*	(2/3, 1/3, 0)	Ge6	2h	(1/3, 2/3, *z*)	Ge4	1*b*	(0, 0, 1/2)
			Ge5	6*k*	(*x*, y, 1/4)	Ge5	6*j*	(*x*, 2x, 0)	Ge7	6n	(*x*, 2x, *z*)	Ge5	1e	(2/3, 1/3, 0)
			Ge6	6*k*	(*x*, y, 1/4)	Ge6	6*j*	(*x*, 2x, 1/2)	Ge8	6n	(*x*, 2x, *z*)	Ge6	1f	(2/3, 1/3, 1/2)
												Ge7	3j	(*x*, 2x, 0)
												Ge8	3j	(*x*, 2x, 0)
												Ge9	3k	(*x*, 2x, 1/2)
												Ge10	3k	(*x*, 2x, 1/2)
Fe	3*f*	(1/2, 0, 0)	Fe1	6*j*	(*x*, 2x, 0)	Fe1	6*k*	(*x*, y, 1/4)	Fe1	3j	(*x*, 2x, 0)	Fe1	6n	(*x*, 2x,*z*)
			Fe2	6*j*	(*x*, 2x, 0)	Fe2	6*k*	(*x*, *y*, 1/4)	Fe2	3j	(*x*, 2x, 0)	Fe2	6n	(*x*, 2x,*z*)
			Fe3	12*l*	(*x*, *y*, *z*)	Fe3	6*k*	(*x*, y, 1/4)	Fe3	3k	(*x*, 2x, 1/2)	Fe3	12o	(*x*, *y*, *z*)
						Fe4	6*k*	(*x*, *y*, 1/4)	Fe4	3k	(*x*, 2x, 1/2)			
									Fe5	6*l*	(*x*, *y*, 0)			
									Fe6	6*m*	(*x*, *y*, 1/2)			

TABLE XII. The corresponding Wyckoff positions and the coordinates of the atoms in the pristine phase and CDW phases with different symmetries. (Part II.)

Pristine phase ($P6/mmm$)			SG186-$P\bar{6}_3mc$ (type I)			SG185-$P\bar{6}_3cm$ (type I)			SG184-$P6cc$ (type I)			SG183-$P6m$m(type I)		
	WP	Coordinates		WP	Coordinates		WP	Coordinates		WP	Coordinates		WP	Coordinates
Ge1	1a	(0, 0, 0)	Ge1	2a	(0, 0, z)	Ge1	2a	(0, 0, z)	Ge1	2a	(0, 0, z)	Ge1	1a	(0, 0, z)
			Ge2	6c	(x, 0, z)	Ge2	6c	(x, 2x, z)	Ge2	6c	(1/2, 0, z)	Ge2	1a	(0, 0, z)
												Ge3	3c	(1/2, 0, z)
												Ge4	3c	(1/2, 0, z)
Ge2	2d	(1/3, 2/3, 1/2)	Ge3	4b	(1/3, 2/3, z)	Ge3	2b	(1/3, 2/3, z)	Ge3	4b	(1/3, 2/3, z)	Ge5	2b	(1/3, 2/3, z)
			Ge4	12d	(x, y, z)	Ge4	2b	(1/3, 2/3, z)	Ge4	12d	(x, y, z)	Ge6	2b	(1/3, 2/3, z)
						Ge5	6c	(x, 2x, z)				Ge7	6e	(x, 2x, z)
						Ge6	6c	(x, 2x, z)				Ge8	6e	(x, 2x, z)
Fe	3f	(1/2, 0, 0)	Fe1	6c	(x, 0, z)	Fe1	6c	(x, 2x, z)	Fe1	12d	(x, y, z)	Fe1	6d	(x, 0, z)
			Fe2	6c	(x, 0, z)	Fe2	6c	(x, 2x, z)	Fe2	12d	(x, y, z)	Fe2	6d	(x, 0, z)
			Fe3	12d	(x, y, z)	Fe3	12d	(x, y, z)				Fe3	6d	(x, 2x, z)
												Fe4	6d	(x, 2x, z)

Pristine phase ($P6/mmm$)			SG182-$P6_322$ (type I)			SG182-$P6_322$ (type II)			SG177-$P622$ (type I)			SG177-P622(type II)		
	WP	Coordinates		WP	Coordinates		WP	Coordinates		WP	Coordinates		WP	Coordinates
Ge1	1a	(0, 0, 0)	Ge1	2a	(0, 0, 0)	Ge1	2b	(0, 0, 1/4)	Ge1	1a	(0, 0, 0)	Ge1	2e	(0, 0, z)
			Ge2	6g	(x, 0, 0)	Ge2	6h	(x, 2x, 1/4)	Ge2	1b	(0, 0, 1/2)	Ge2	6i	(1/2, 0, z)
									Ge3	3f	(0, 1/2, 0)			
									Ge4	3g	(0, 1/2, 1/2)			
Ge2	2d	(1/3, 2/3, 1/2)	Ge3	2c	(1/3, 2/3, 1/4)	Ge3	4f	(1/3, 2/3, z)	Ge5	4h	(1/3, 2/3, z)	Ge3	2c	(1/3, 2/3, 0)
			Ge4	2d	(1/3, 2/3, 3/4)	Ge4	12i	(x, y, z)	Ge6	12n	(x, y, z)	Ge4	2d	(1/3, 2/3,1/2)
			Ge5	6h	(x, 2x, 1/4)							Ge5	6l	(x, 2x, 0)
			Ge6	6h	(x, 2x, 1/4)							Ge6	6m	(x, 2x, 1/2)
Fe	3f	(1/2, 0, 0)	Fe1	6g	(x, 0, 0)	Fe1	6h	(x, 2x, 1/4)	Fe1	6j	(x, 0, 0)	Fe1	12n	(x, y, z)
			Fe2	6g	(x, 0, 0)	Fe2	6h	(x, 2x, 1/4)	Fe2	6k	(x, 0, 1/2)	Fe1	12n	(x, y, z)
			Fe3	12i	(x, y, z)	Fe3	12i	(x, y, z)	Fe3	6l	(x, 2x, 0)			
									Fe4	6m	(x, 2x, 1/2)			

Pristine phase ($P6/mmm$)			SG176-$P6_3/m$ (type I)			SG176-$P6_3/m$ (type II)			SG175-$P6/m$ (type I)			SG175-P6/m(type II)		
	WP	Coordinates		WP	Coordinates		WP	Coordinates		WP	Coordinates		WP	Coordinates
Ge1	1a	(0, 0, 0)	Ge1	2b	(0, 0, 0)	Ge1	2a	(0, 0, 1/4)	Ge1	1a	(0, 0, 0)	Ge1	2e	(0, 1/2, z)
			Ge2	6g	(1/2, 0, 0)	Ge2	6h	(x, y, 1/4)	Ge2	1b	(0, 0, 1/2)	Ge2	6i	(0, 0, z)
									Ge3	3f	(1/2, 0, 0)			
									Ge4	3g	(1/2, 0, 1/2)			
Ge2	2d	(1/3, 2/3, 1/2)	Ge3	2c	(1/3, 2/3, 1/4)	Ge3	4f	(1/3, 2/3, z)	Ge5	4h	(1/3, 2/3, z)	Ge3	2c	(1/3, 2/3, 0)
			Ge4	2d	(1/3, 2/3, 3/4)	Ge4	12i	(x, y, z)	Ge6	212l	(x, y, z)	Ge4	2d	(1/3, 2/3, 1/2)
			Ge5	6h	(x, y, 1/4)							Ge5	6j	(x, y, 0)
			Ge6	6h	(x, y, 1/4)							Ge6	6k	(x, y, 1/2)
Fe	3f	(1/2, 0, 0)	Fe1	12i	(x, y, z)	Fe1	6h	(x, y, 1/4)	Fe1	6j	(x, y, 0)	Fe1	12l	(x, y, z)
			Fe2	12i	(x, y, z)	Fe2	6h	(x, y, 1/4)	Fe2	6j	(x, y, 0)	Fe2	12l	(x, y, z)
						Fe3	6h	(x, y, 1/4)	Fe3	6k	(x, y, 1/2)			
						Fe4	6h	(x, y, 1/4)	Fe4	6k	(x, y, 1/2)			

Pristine phase(P6/mmm)			SG165-P$\bar{3}$c1(type I)			SG165-P$\bar{3}$c1(type II)			SG164-P$\bar{3}$ m1(type I)			SG164-P $\bar{3}$m1(type II)		
	WP	Coordinates		WP	Coordinates		WP	Coordinates		WP	Coordinates		WP	Coordinates
Ge1	1a	(0, 0, 0)	Ge1	2b	(0, 0, 0)	Ge1	2a	(0, 0, 1/4)	Ge1	1a	(0, 0, 0)	Ge1	2c	(0, 0, z)
			Ge2	6e	(1/2, 0, 0)	Ge2	6f	(x, 0, 1/4)	Ge2	1b	(0, 0, 1/2)	Ge2	6i	(x, 2x z)
									Ge3	3e	(0, 1/2, 0)			
									Ge4	3f	(0, 1/2, 1/2)			
Ge2	2d	(1/3, 2/3, 1/2)	Ge3	4d	(1/3, 2/3, z)	Ge3	4d	(1/3, 2/3, z)	Ge5	2d	(1/3, 2/3, z)	Ge3	2d	(1/3, 2/3, z)
			Ge4	12g	(x, y, z)	Ge4	12g	(x, y, z)	Ge6	2d	(1/3, 2/3, z)	Ge4	2d	(1/3, 2/3, z)
									Ge7	6i	(x, 2x, z)	Ge5	6i	(x, 2x, z)
									Ge8	6i	(x, 2x, z)	Ge6	6i	(x, 2x, z)
Fe	3f	(1/2, 0, 0)	Fe1	12g	(x, y, z)	Fe1	6f	(x, 0, 1/4)	Fe1	6i	(x, 2x, z)	Fe1	6i	(x, 2x, z)
			Fe2	12g	(x, y, z)	Fe2	6f	(x, 0, 1/4)	Fe2	6i	(x, 2x, z)	Fe2	6i	(x, 2x, z)
						Fe3	12g	(x, y, z)	Fe3	12j	(x, y, z)	Fe3	12j	(x, y, z)

TABLE XIII. The corresponding Wyckoff positions and the coordinates of the atoms in the pristine phase and CDW phases with different symmetries. (Part III.)

Pristine phase ($P6/mmm$)			SG163-$P\bar{3}1c$ (type I)			SG163-P$\bar{3}$1c (type II)			SG162-P$\bar{3}$ 1m (type I)			SG162-P $\bar{3}$1m(type II)		
	WP	Coordinates		WP	Coordinates		WP	Coordinates		WP	Coordinates		WP	Coordinates
Ge1	1*a*	(0, 0, 0)	Ge1	2*b*	(0, 0, 0)	Ge1	2*a*	(0, 0, 1/4)	Ge1	1*a*	(0, 0, 0)	Ge1	2*e*	(0, 0, *z*)
			Ge2	6*g*	(0, 1/2, 0)	Ge2	6*h*	(*x*, 2x, 1/4)	Ge2	1*b*	(0, 0, 1/2)	Ge2	6*k*	(*x*, 0, *z*)
									Ge3	3*f*	(1/2, 0, 0)			
									Ge4	3*g*,	(1/2, 0, 1/2)			
Ge2	2*d*	(1/3, 2/3, 1/2)	Ge3	2*c*	(1/3, 2/3, 1/4)	Ge3	4*f*	(1/3, 2/3, *z*)	Ge5	4*h*	(1/3, 2/3, *z*)	Ge3	2*c*	(1/3, 2/3, 0)
			Ge4	2*d*	(1/3, 2/3, 3/4)	Ge4	12*i*	(*x*, *y*, *z*)	Ge6	12*l*	(*x*, *y*, *z*)	Ge4	2*d*	(1/3, 2/3, 1/2)
			Ge5	6*h*	(*x*, 2x, 1/4)							Ge5	6*i*	(*x*, 2x, 0)
			Ge6	6*h*	(*x*, 2x, 1/4)							Ge6	6*j*	(*x*, 2x, 1/2)
Fe	3*f*	(1/2, 0, 0))	Fe1	12*i*	(*x*, *y*, *z*)	Fe1	6*h*	(*x*, 2x, 1/4)	Fe1	6*i*	(*x*, 2x, 0)	Fe1	6*k*	(*x*, 0, *z*)
			Fe2	12*i*	(*x*, *y*, *z*)	Fe2	6*h*	(*x*, 2x, 1/4)	Fe2	6*j*	(*x*, 2x, 1/2)	Fe2	6*k*	(*x*, 0, *z*)
						Fe3	12*i*	(*x*, *y*, *z*)	Fe3	6*k*	(*x*, 0, *z*)	Fe3	12*i*	(*x*, *y*, *z*)
									Fe4	6*k*	(*x*, 0, *z*)			

Pristine phase ($P6/mmm$)			SG68-*Ccce* (type I)			SG68-*Ccce* (type II)			SG68-*Ccce* (type III)			SG68-Ccce(type IV)		
	WP	Coordinates		WP	Coordinates		WP	Coordinates		WP	Coordinates		WP	Coordinates
Ge1	1*a*	(0, 0, 0)	Ge1	8*c*	(1/4, 1/4, 0)	Ge1	8*e*	(*x*, 1/4, 1/4)	Ge1	8*g*	(0, 1/4, *z*)	Ge1	4*a*	(0, 1/4, 1/4)
			Ge2	8*d*	(0, 0, 0)	Ge2	8*f*	(0, *y*, 1/4)	Ge2	8*h*	(1/4, 0, *z*)	Ge2	4*b*	(0, 1/4, 3/4)
												Ge3	8*h*	(1/4, 0, *z*)
Ge2	2*d*	(1/3, 2/3, 1/2)	Ge3	8*f*	(0, *y*, 1/4)	Ge3	16*i*	(*x*, *y*, *z*)	Ge3	8*f*	(0, *y*, 1/4)	Ge3	16*i*	(*x*, *y*, *z*)
			Ge4	8*f*	(0, *y*, 1/4)	Ge4	16*i*	(*x*, *y*, *z*)	Ge4	8*f*	(0, *y*, 1/4)	Ge4	16*i*	(*x*, *y*, *z*)
			Ge5	16*i*	(*x*, *y*, *z*)				Ge5	16*i*	(*x*, *y*, *z*)			
Fe	3*f*	(1/2, 0, 0))	Fe1	8*g*	(0, 1/4, *z*)	Fe1	4*a*	(0, 1/4, 1/4)	Fe1	8*c*	(1/4, 1/4, 0)	Fe1	8*e*	(*x*, 1/4, 1/4)
			Fe2	8*h*	(1/4, 0, *z*)	Fe2	4*b*	(0, 1/4, 3/4)	Fe2	8*d*	(0, 0, 1/2)	Fe2	8*f*	(0, *y*, 1/4)
			Fe3	16*i*	(*x*, *y*, *z*)	Fe3	8*h*	(1/4, 0, *z*)	Fe3	16*i*	(*x*, *y*, *z*)	Fe3	16*i*	(*x*, *y*, *z*)
			Fe4	16*i*	(*x*, *y*, *z*)	Fe4	16*i*	(*x*, *y*, *z*)	Fe4	16*i*	(*x*, *y*, *z*)	Fe4	16*i*	(*x*, *y*, *z*)
						Fe5	16*i*	(*x*, *y*, *z*)						

Pristine phase ($P6/mmm$)			SG67-*Cmme* (type I)			SG67-*Cmme* (type II)			SG67-*Cmme* (type III)			SG67-Cmme(type IV)		
	WP	Coordinates		WP	Coordinates		WP	Coordinates		WP	Coordinates		WP	Coordinates
Ge1	1*a*	(0, 0, 0)	Ge1	4*c*	(0, 0, 0)	Ge1	4*a*	(1/4, 0, 0)	Ge1	4*g*	(0, 1/4, *z*)	Ge1	8*n*	(*x*, 1/4, *z*)
			Ge2	4*d*	(0, 0, 1/2)	Ge2	4*b*	(1/4, 0, 1/2)	Ge2	4*g*	(0, 1/4, *z*)	Ge2	8*m*	(0, *y*, *z*)
			Ge3	4*e*	(1/4, 1/4, 0)	Ge3	4*g*	(0, 1/4, *z*)	Ge3	8l	(1/4, 0, *z*)			
			Ge4	4*f*	(1/4, 1/4, 1/2)	Ge4	4*g*	(0, 1/4, *z*)						
Ge2	2*d*	(1/3, 2/3, 1/2)	Ge5	8*m*	(0, *y*, *z*)	Ge5	8*m*	(0, *y*, *z*)	Ge4	8j	(1/4, *y*, 0)	Ge3	8j	(1/4, *y*, 0)
			Ge6	8*m*	(0, *y*, *z*)	Ge6	8*m*	(0, *y*, *z*)	Ge5	8k	(1/4, *y*, 1/2)	Ge4	8k	(1/4, *y*, 1/2)
			Ge7	16o	(*x*, *y*, *z*)	Ge7	16o	(*x*, *y*, *z*)	Ge6	8*m*	(0, *y*, *z*)	Ge5	8*m*	(0, *y*, *z*)
									Ge7	8*m*	(0, *y*, *z*)	Ge6	8*m*	(0, *y*, *z*)
Fe	3*f*	(1/2, 0, 0))	Fe1	4*a*	(1/4, 0, 0)	Fe1	4*c*	(0, 0, 0)	Fe1	8*n*	(*x*, 1/4, *z*)	Fe1	4*g*	(0, 1/4, *z*)
			Fe2	4*b*	(1/4, 0, 1/2)	Fe2	4*d*	(0, 0, 1/2)	Fe2	8*m*	(0, *y*, *z*)	Fe2	4*g*	(0, 1/4, *z*)
			Fe3	4*g*	(0, 1/4, *z*)	Fe3	4*e*	(1/4, 1/4, 0)	Fe3	16o	(*x*, *y*, *z*)	Fe3	8l	(1/4, 0, *z*)
			Fe4	4*g*	(0, 1/4, *z*)	Fe4	4*f*	(1/4, 1/4, 1/2)	Fe4	16o	(*x*, *y*, *z*)	Fe4	16o	(*x*, *y*, *z*)
			Fe5	16o	(*x*, *y*, *z*)	Fe5	16o	(*x*, *y*, *z*)				Fe5	16o	(*x*, *y*, *z*)
			Fe6	16o	(*x*, *y*, *z*)	Fe6	16o	(*x*, *y*, *z*)						

Pristine phase(P6/mmm)			SG66-Cccm(type I)			SG66-Cccm(type II)			SG66-Cccm(type III)			SG66-Cccm(type IV)		
	WP	Coordinates		WP	Coordinates		WP	Coordinates		WP	Coordinates		WP	Coordinates
Ge1	1*a*	(0, 0, 0)	Ge1	4*c*	(0, 0, 0)	Ge1	4*a*	(0, 0, 1/4)	Ge1	8l	(*x*, *y*, 0)	Ge1	8*g*	(*x*, 0, 1/4)
			Ge2	4*d*	(0, 0, 1/2)	Ge2	4*b*	(0, 1/2, 1/4)	Ge2	8l	(*x*, *y*, 0)	Ge2	8*h*	(0, *y*, 1/4)
			Ge3	4*e*	(1/4, 1/4, 0)	Ge3	8k	(1/4, 1/4, 1/4)						
			Ge4	4*f*	(1/4, 1/4, 1/2)									
Ge2	2*d*	(1/3, 2/3, 1/2)	Ge5	8*h*	(0, *y*, 1/4)	Ge4	8l	(*x*, *y*, 0)	Ge3	8*h*	(0, *y*, 1/4)	Ge3	8l	(*x*, *y*, 0)
			Ge6	8*h*	(0, *y*, 1/4)	Ge5	8l	(*x*, *y*, 0)	Ge4	8*h*	(0, *y*, 1/4)	Ge4	8l	(*x*, *y*, 0)
			Ge7	16*m*	(*x*, *y*, *z*)	Ge6	8l	(*x*, *y*, 0)	Ge5	16*m*	(*x*, *y*, *z*)	Ge5	8l	(*x*, *y*, 0)
						Ge7	8l	(*x*, *y*, 0)				Ge6	8l	(*x*, *y*, 0)
Fe	3*f*	(1/2, 0, 0))	Fe1	8l	(*x*, *y*, 0)	Fe1	8*g*	(*x*, 0, 1/4)	Fe1	4*c*	(0, 0, 0)	Fe1	4*a*	(0, 0, 1/4)
			Fe2	8l	(*x*, *y*, 0)	Fe2	8*h*	(0, *y*, 1/4)	Fe2	4*d*	(0, 0, 1/2)	Fe2	4*b*	(0, 1/2, 1/4)
			Fe3	8l	(*x*, *y*, 0)	Fe3	16*m*	(*x*, *y*, *z*)	Fe3	4*e*	(1/4, 1/4, 0)	Fe3	8k	(1/4, 1/4, 1/4)
			Fe4	8l	(*x*, *y*, 0)	Fe4	16*m*	(*x*, *y*, *z*)	Fe4	4*f*	(1/4, 1/4, 1/2)	Fe4	16*m*	(*x*, *y*, *z*)
			Fe5	8l	(*x*, *y*, 0)				Fe5	8l	(*x*, *y*, 0)	Fe5	16*m*	(*x*, *y*, *z*)
			Fe6	8l	(*x*, *y*, 0)				Fe6	8l	(*x*, *y*, 0)			
									Fe7	8l	(*x*, *y*, 0)			
									Fe8	8l	(*x*, *y*, 0)			

TABLE XIV. The corresponding Wyckoff positions and the coordinates of the atoms in the pristine phase and CDW phases with different symmetries. (Part IV.)

Pristine phase (*P*6/*mmm*)			SG65-*Cmmm* (type I)			SG65-*Cmmm* (type II)			SG65-*Cmmm* (type III)			SG65-Cmmm(type IV)		
	WP	Coordinates		WP	Coordinates		WP	Coordinates		WP	Coordinates		WP	Coordinates
Ge1	1*a*	(0, 0, 0)	Ge1	2*a*	(0, 0, 0)	Ge1	4*i*	(0, *y*, 0)	Ge1	4*k*	(0, 0, *z*)	Ge1	8*o*	(*x*, 0, *z*)
			Ge2	2*b*	(0, 1/2, 0)	Ge2	4*j*	(0, *y*, 1/2)	Ge2	4*l*	(0, 1/2, *z*)	Ge2	8*n*	(0, *y*, *z*)
			Ge3	2*c*	(0, 1/2, 1/2)	Ge3	4*g*	(*x*, 0, 0)	Ge3	8*m*	(1/4, 1/4, *z*)			
			Ge4	2*d*	(0, 0, 1/2)	Ge4	4*h*	(*x*, 0, 1/2)						
			Ge5	4*e*	(1/4, 1/4, 0)									
			Ge6	4*f*	(1/4, 1/4, 1/2)									
Ge2	2*d*	(1/3, 2/3, 1/2)	Ge7	8*n*	(0, *y*, *z*)	Ge5	8*n*	(0, *y*, *z*)	Ge4	4*i*	(0, *y*, 0)	Ge3	4*i*	(0, *y*, 0)
			Ge8	8*n*	(0, *y*, *z*)	Ge6	8*n*	(0, *y*, *z*)	Ge5	4*i*	(0, *y*, 0)	Ge4	4*i*	(0, *y*, 0)
			Ge9	16*r*	(*x*, *y*, *z*)	Ge7	16*r*	(*x*, *y*, *z*)	Ge6	4*j*	(0, *y*, 1/2)	Ge5	4*j*	(0, *y*, 1/2)
									Ge7	4*j*	(0, *y*, 1/2)	Ge6	4*j*	(0, *y*, 1/2)
									Ge8	8*p*	(*x*, *y*, 0)	Ge7	8*p*	(*x*, *y*, 0)
									Ge9	8*q*	(*x*, *y*, 1/2)	Ge8	8*q*	(*x*, *y*, 1/2)
Fe	3*f*	(1/2, 0, 0)	Fe1	4*g*	(*x*, 0, 0)	Fe1	2*a*	(0, 0, 0)	Fe1	8*o*	(*x*, 0, *z*)	Fe1	4*k*	(0, 0, *z*)
			Fe2	4*h*	(*x*, 0, 1/2)	Fe2	2*b*	(0, 1/2, 0)	Fe2	8*n*	(0, *y*, *z*)	Fe2	4*l*	(0, 1/2, *z*)
			Fe3	4*i*	(0, *y*, 0)	Fe3	2*c*	(0, 1/2, 1/2)	Fe3	16*r*	(*x*, *y*, *z*)	Fe3	8*m*	(1/4, 1/4, *z*)
			Fe4	4*j*	(0, *y*, 1/2)	Fe4	2*d*	(0, 0, 1/2)	Fe4	16*r*	(*x*, *y*, *z*)	Fe4	16*r*	(*x*, *y*, *z*)
			Fe5	8*p*	(*x*, *y*, 0)	Fe5	4*e*	(1/4, 1/4, 0)				Fe5	16*r*	(*x*, *y*, *z*)
			Fe6	8*p*	(*x*, *y*, 0)	Fe6	4*f*	(1/4, 1/4, 1/2)						
			Fe7	8*q*	(*x*, *y*, 1/2)	Fe7	8*p*	(*x*, *y*, 0)						
			Fe8	8*q*	(*x*, *y*, 1/2)	Fe8	8*p*	(*x*, *y*, 0)						
						Fe9	8*q*	(*x*, *y*, 1/2)						
						Fe10	8*q*	(*x*, *y*, 1/2)						

Pristine phase (*P*6/*mmm*)			SG64-*Cmce* (type I)			SG64-*Cmce* (type II)			SG64-*Cmce* (type III)			SG64-*Cmce* (type IV)		
	WP	Coordinates		WP	Coordinates		WP	Coordinates		WP	Coordinates		WP	Coordinates
Ge1	1*a*	(0, 0, 0)	Ge1	4*a*	(0, 0, 0)	Ge1	4*a*	(0, 0, 0)	Ge1	8*e*	(1/4, *y*, 1/4)	Ge1	8*e*	(1/4, *y*, 1/4)
			Ge2	4*b*	(0, 0, 1/2)	Ge2	4*b*	(0, 0, 1/2)	Ge2	8*f*	(0, *y*, *z*)	Ge2	8*f*	(0, *y*, *z*)
			Ge3	8*c*	(1/4, 1/4, 0)	Ge3	8*c*	(1/4, 1/4, 0)						
Ge2	2*d*	(1/3, 2/3, 1/2)	Ge4	16*g*	(*x*, *y*, *z*)	Ge4	8*e*	(1/4, *y*, 1/4)	Ge3	8*d*	(*x*, 0, 0)	Ge3	8*f*	(0, *y*, *z*)
			Ge5	16*g*	(*x*, *y*, *z*)	Ge5	8*e*	(1/4, *y*, 1/4)	Ge4	8*d*	(*x*, 0, 0)	Ge4	8*f*	(0, *y*, *z*)
						Ge6	8*f*	(0, *y*, *z*)	Ge5	16*g*	(*x*, *y*, *z*)	Ge5	16*g*	(*x*, *y*, *z*)
						Ge7	8*f*	(0, *y*, *z*)						
Fe	3*f*	(1/2, 0, 0))	Fe1	8*d*	(*x*, 0, 0)	Fe1	8*e*	(1/4, *y*, 1/4)	Fe1	8*e*	(1/4, *y*, 1/4)	Fe1	8*e*	(1/4, *y*, 1/4)
			Fe2	8*f*	(0, *y*, *z*)	Fe2	8*f*	(0, *y*, *z*)	Fe2	8*f*	(0, *y*, *z*)	Fe2	8*f*	(0, *y*, *z*)
			Fe3	16*g*	(*x*, *y*, *z*)	Fe3	16*g*	(*x*, *y*, *z*)	Fe3	16*g*	(*x*, *y*, *z*)	Fe3	16*g*	(*x*, *y*, *z*)
			Fe4	16*g*	(*x*, *y*, *z*)	Fe4	16*g*	(*x*, *y*, *z*)	Fe4	16*g*	(*x*, *y*, *z*)	Fe4	16*g*	(*x*, *y*, *z*)

Pristine phase(P6/mmm)			SG64-Cmce(type V)			SG64-Cmce(type VI)			SG64-Cmce(type VII)			SG64-Cmce(type VIII)		
	WP	Coordinates		WP	Coordinates		WP	Coordinates		WP	Coordinates		WP	Coordinates
Ge1	1*a*	(0, 0, 0)	Ge1	8*e*	(1/4, *y*, 1/4)	Ge1	8*e*	(1/4, *y*, 1/4)	Ge1	8*d*	(*x*, 0, 0)	Ge1	8*d*	(*x*, 0, 0)
			Ge2	8*f*	(0, *y*, *z*)	Ge2	8*f*	(0, *y*, *z*)	Ge2	8*f*	(0, *y*, *z*)	Ge2	8*f*	(0, *y*, *z*)
Ge2	2*d*	(1/3, 2/3, 1/2)	Ge3	8*f*	(0, *y*, *z*)	Ge3	8*d*	(*x*, 0, 0)	Ge3	16*g*	(*x*, *y*, *z*)	Ge4	8*e*	(1/4, *y*, 1/4)
			Ge4	8*f*	(0, *y*, *z*)	Ge4	8*d*	(*x*, 0, 0)	Ge4	16*g*	(*x*, *y*, *z*)	Ge5	8*e*	(1/4, *y*, 1/4)
			Ge5	16*g*	(*x*, *y*, *z*)	Ge5	16*g*	(*x*, *y*, *z*)				Ge6	8*f*	(0, *y*, *z*)
												Ge7	8*f*	(0, *y*, *z*)
Fe	3*f*	(1/2, 0, 0))	Fe1	8*e*	(1/4, *y*, 1/4)	Fe1	8*e*	(1/4, *y*, 1/4)	Fe1	4*a*	(0, 0, 0)	Fe1	4*a*	(0, 0, 0)
			Fe2	8*f*	(0, *y*, *z*)	Fe2	8*f*	(0, *y*, *z*)	Fe2	4*b*	(0, 0, 1/2)	Fe2	4*b*	(0, 0, 1/2)
			Fe3	16*g*	(*x*, *y*, *z*)	Fe3	16*g*	(*x*, *y*, *z*)	Fe3	8*c*	(1/4, 1/4, 0)	Fe3	8*c*	(1/4, 1/4, 0)
			Fe4	16*g*	(*x*, *y*, *z*)	Fe4	16*g*	(*x*, *y*, *z*)	Fe4	16*g*	(*x*, *y*, *z*)	Fe4	16*g*	(*x*, *y*, *z*)
									Fe5	16*g*	(*x*, *y*, *z*)	Fe5	16*g*	(*x*, *y*, *z*)

interactions in pairs. For example, as shown in Table IX, the $\mathbf{D}_{c2,1}$ and $\mathbf{D}_{c2,7}$ are connected by the inversion symmetry and have opposite values. Therefore, the summation over equivalent interlayer DM interactions are all zero due to the inversion symmetry. Note that not only inversion symmetry but mirror symmetries such as $\{m_{001}|0\}$, $\{m_{110}|0\}$, $\{m_{100}|0\}$, $\{m_{010}|0\}$, $\{m_{1-10}|0\}$, $\{m_{120}|0\}$, and $\{m_{210}|0\}$ in space group *P*6/*mmm*, would also make the DM contributions to the canted

TABLE XV. The corresponding Wyckoff positions and the coordinates of the atoms in the pristine phase and CDW phases with different symmetries. (Part V.)

Pristine phase ($P6/mmm$)			SG63-$Cmcm$ (type I)			SG63-$Cmcm$ (type II)			SG63-$Cmcm$ (type III)			SG63-Cmcm(type IV)		
	WP	Coordinates		WP	Coordinates		WP	Coordinates		WP	Coordinates		WP	Coordinates
Ge1	1a	(0, 0, 0)	Ge1	4a	(0, 0, 0)	Ge1	4a	(0, 0, 0)	Ge1	4c	(0, y, 1/4)	Ge1	4c	(0, y, 1/4)
			Ge2	4b	(0, 1/2, 0)	Ge2	4b	(0, 1/2, 0)	Ge2	4c	(0, y, 1/4)	Ge2	4c	(0, y, 1/4)
			Ge3	8d	(1/4, 1/4, 0)	Ge3	8d	(1/4, 1/4, 0)	Ge3	8g	(x, y, 1/4)	Ge3	8g	(x, y, 1/4)
Ge2	2d	(1/3, 2/3, 1/2)	Ge4	8g	(x, y, 1/4)	Ge4	4c	(0, y, 1/4)	Ge4	8e	(x, 0, 0)	Ge4	8e	(x, 0, 0)
			Ge5	8g	(x, y, 1/4)	Ge5	4c	(0, y, 1/4)	Ge5	8e	(x, 0, 0)	Ge5	8e	(x, 0, 0)
			Ge6	8g	(x, y, 1/4)	Ge6	4c	(0, y, 1/4)	Ge6	16h	(x, y, z)	Ge6	16h	(x, y, z)
			Ge7	8g	(x, y, 1/4)	Ge7	4c	(0, y, 1/4)						
						Ge8	8g	(x, y, 1/4)						
						Ge9	8g	(x, y, 1/4)						
Fe	3f	(1/2, 0, 0)	Fe1	8e	(x, 0, 0)	Fe1	8e	(x, 0, 0)	Fe1	4c	(0, y, 1/4)	Fe1	4c	(0, y, 1/4)
			Fe2	8f	(0, y, z)	Fe2	8f	(0, y, z)	Fe2	4c	(0, y, 1/4)	Fe2	4c	(0, y, 1/4)
			Fe3	16h	(x, y, z)	Fe3	16h	(x, y, z)	Fe3	8g	(x, y, 1/4)	Fe3	8g	(x, y, 1/4)
			Fe4	16h	(x, y, z)	Fe4	16h	(x, y, z)	Fe4	8g	(x, y, 1/4)	Fe4	8g	(x, y, 1/4)
									Fe5	8g	(x, y, 1/4)	Fe5	8g	(x, y, 1/4)
									Fe6	8g	(x, y, 1/4)	Fe6	8g	(x, y, 1/4)
									Fe7	8g	(x, y, 1/4)	Fe7	8g	(x, y, 1/4)

Pristine phase ($P6/mmm$)			SG63-$Cmcm$ (type V)			SG63-$Cmcm$ (type VI)			SG63-$Cmcm$ (type VII)			SG63-$Cmcm$ (type VIII)		
	WP	Coordinates		WP	Coordinates		WP	Coordinates		WP	Coordinates		WP	Coordinates
Ge1	1a	(0, 0, 0)	Ge1	4c	(0, y, 1/4)	Ge1	4c	(0, y, 1/4)	Ge1	8e	(x, 0, 0)	Ge1	8e	(x, 0, 0)
			Ge2	4c	(0, y, 1/4)	Ge2	4c	(0, y, 1/4)	Ge2	8f	(0, y, z)	Ge2	8f	(0, y, z)
			Ge3	8g	(x, y, 1/4)	Ge3	8g	(x, y, 1/4)						
Ge2	2d	(1/3, 2/3, 1/2)	Ge4	8f	(0, y, z)	Ge4	8f	(0, y, z)	Ge3	8g	(x, y, 1/4)	Ge4	4c	(0, y, 1/4)
			Ge5	8f	(0, y, z)	Ge5	8f	(0, y, z)	Ge4	8g	(x, y, 1/4)	Ge5	4c	(0, y, 1/4)
			Ge6	16h	(x, y, z)	Ge6	16h	(x, y, z)	Ge5	8g	(x, y, 1/4)	Ge6	4c	(0, y, 1/4)
									Ge6	8g	(x, y, 1/4)	Ge7	4c	(0, y, 1/4)
												Ge8	8g	(x, y, 1/4)
												Ge9	8g	(x, y, 1/4)
Fe	3f	(1/2, 0, 0))	Fe1	4c	(0, y, 1/4)	Fe1	4c	(0, y, 1/4)	Fe1	4a	(0, 0, 0)	Fe1	4a	(0, 0, 0)
			Fe2	4c	(0, y, 1/4)	Fe2	4c	(0, y, 1/4)	Fe2	4b	(0, 1/2, 0)	Fe2	4b	(0, 1/2, 0)
			Fe3	8g	(x, y, 1/4)	Fe3	8g	(x, y, 1/4)	Fe3	8d	(1/4, 1/4, 0)	Fe3	8d	(1/4, 1/4, 0)
			Fe4	8g	(x, y, 1/4)	Fe4	8g	(x, y, 1/4)	Fe4	16h	(x, y, z)	Fe4	16h	(x, y, z)
			Fe5	8g	(x, y, 1/4)	Fe5	8g	(x, y, 1/4)	Fe5	16h	(x, y, z)	Fe5	16h	(x, y, z)
			Fe6	8g	(x, y, 1/4)	Fe6	8g	(x, y, 1/4)						
			Fe7	8g	(x, y, 1/4)	Fe7	8g	(x, y, 1/4)						

magnetic ground state to be zero based on the similar analysis above. Therefore, DM interactions have no contribution to double cone magnetic structure with the symmetry of high-temperature phase.

As mentioned in the main text, since the $2 \times 2 \times 2$ supercell structure of the CDW phase (compared with the nonmagnetic pristine phase) is suggested experimentally [45,46,48,49], we present the possible CDW phases of kagome FeGe with $2 \times 2 \times 2$ supercell. The $2 \times 2 \times 2$ supercell without distortion has the symmetry of space group $P6/mmm$, the nonprimitive translation operations t_x $\{1|1/2,0,0\}$, t_y $\{1|0,1/2,0\}$, t_z $\{1|0,0,1/2\}$, and many symmetry operations from their combinations. As the subgroups compatible with $2 \times 2 \times 2$ supercell of pristine FeGe, the structural distortion of CDW phases would break the nonprimitive translation operations t_x, t_y, and t_z, and possibly break other symmetry operations as well. Since the point group associated with high-temperature phase FeGe ($P6/mmm$) is D_{6h}, we consider all CDW phases whose associated point group is D_{6h} itself or in maximal subgroups of D_{6h} (D_{2h}, D_6, C_{6h}, C_{6v}, D_{3d}, D_{3h}). In total, we find 68 different possible CDW phases and list the corresponding relations of atomic positions in the high-temperature phase and all types of proposed CDW phases in Tables XI–XV. Note that the inversion symmetry and mirror symmetries in parent group $P6/mmm$ would all eliminate the contribution of DM interactions based on the symmetry analysis. Among these 68 proposed CDW phases, only four distorted structures do not have the inversion symmetry and mirror symmetries, which can lead to nonzero DM contribution to the double cone spin structure and may explain this magnetic ground state. They belong to two space groups $P622$ and $P6_322$, and we list the corresponding Wyckoff positions and the coordinates of the atoms in the pristine phase and these four CDW phases in Table II of the main text.

[1] I. Syôzi, Statistics of kagomé lattice, Prog. Theor. Phys. **6**, 306 (1951).

[2] A. Mielke, Ferromagnetic ground states for the Hubbard model on line graphs, J. Phys. A: Math. Gen. **24**, L73 (1991).

[3] A. Tanaka and H. Ueda, Stability of Ferromagnetism in the Hubbard Model on the Kagome Lattice, Phys. Rev. Lett. **90**, 067204 (2003).

[4] M. L. Kiesel, C. Platt, and R. Thomale, Unconventional Fermi Surface Instabilities in the Kagome Hubbard Model, Phys. Rev. Lett. **110**, 126405 (2013).

[5] T. Park, M. Ye, and L. Balents, Electronic instabilities of kagome metals: Saddle points and Landau theory, Phys. Rev. B **104**, 035142 (2021).

[6] M. Kang, L. Ye, S. Fang, J.-S. You, A. Levitan, M. Han, J. I. Facio, C. Jozwiak, A. Bostwick, E. Rotenberg, M. K. Chan, R. D. McDonald, D. Graf, K. Kaznatcheev, E. Vescovo, D. C. Bell, E. Kaxiras, J. van den Brink, M. Richter, M. Prasad Ghimire *et al.*, Dirac fermions and flat bands in the ideal kagome metal FeSn, Nat. Mater. **19**, 163 (2020).

[7] Y. Xie, L. Chen, T. Chen, Q. Wang, Q. Yin, J. R. Stewart, M. B. Stone, L. L. Daemen, E. Feng, H. Cao, H. Lei, Z. Yin, A. H. MacDonald, and P. Dai, Spin excitations in metallic kagome lattice FeSn and CoSn, Commun. Phys. **4**, 240 (2021).

[8] B. C. Sales, J. Yan, W. R. Meier, A. D. Christianson, S. Okamoto, and M. A. McGuire, Electronic, magnetic, and thermodynamic properties of the kagome layer compound FeSn, Phys. Rev. Mater. **3**, 114203 (2019).

[9] S.-H. Do, K. Kaneko, R. Kajimoto, K. Kamazawa, M. B. Stone, J. Y. Y. Lin, S. Itoh, T. Masuda, G. D. Samolyuk, E. Dagotto, W. R. Meier, B. C. Sales, H. Miao, and A. D. Christianson, Damped Dirac magnon in the metallic kagome antiferromagnet FeSn, Phys. Rev. B **105**, L180403 (2022).

[10] Y.-F. Zhang, X.-S. Ni, T. Datta, M. Wang, D.-X. Yao, and K. Cao, Ab initio study of spin fluctuations in the itinerant kagome magnet FeSn, Phys. Rev. B **106**, 184422 (2022).

[11] L. Ye, M. Kang, J. Liu, F. von Cube, C. R. Wicker, T. Suzuki, C. Jozwiak, A. Bostwick, E. Rotenberg, D. C. Bell, L. Fu, R. Comin, and J. G. Checkelsky, Massive dirac fermions in a ferromagnetic kagome metal, Nature (London) **555**, 638 (2018).

[12] Z. Lin, J.-H. Choi, Q. Zhang, W. Qin, S. Yi, P. Wang, L. Li, Y. Wang, H. Zhang, Z. Sun, L. Wei, S. Zhang, T. Guo, Q. Lu, J.-H. Cho, C. Zeng, and Z. Zhang, Flatbands and Emergent Ferromagnetic Ordering in Fe_3Sn_2 Kagome Lattices, Phys. Rev. Lett. **121**, 096401 (2018).

[13] N. Morali, R. Batabyal, P. K. Nag, E. Liu, Q. Xu, Y. Sun, B. Yan, C. Felser, N. Avraham, and H. Beidenkopf, Fermi-arc diversity on surface terminations of the magnetic Weyl semimetal $Co_3Sn_2S_2$, Science **365**, 1286 (2019).

[14] D. F. Liu, A. J. Liang, E. K. Liu, Q. N. Xu, Y. W. Li, C. Chen, D. Pei, W. J. Shi, S. K. Mo, P. Dudin, T. Kim, C. Cacho, G. Li, Y. Sun, L. X. Yang, Z. K. Liu, S. S. P. Parkin, C. Felser, and Y. L. Chen, Magnetic Weyl semimetal phase in a Kagomé crystal, Science **365**, 1282 (2019).

[15] K. Kuroda, T. Tomita, M.-T. Suzuki, C. Bareille, A. A. Nugroho, P. Goswami, M. Ochi, M. Ikhlas, M. Nakayama, S. Akebi, R. Noguchi, R. Ishii, N. Inami, K. Ono, H. Kumigashira, A. Varykhalov, T. Muro, T. Koretsune, R. Arita, S. Shin *et al.*, Evidence for magnetic Weyl fermions in a correlated metal, Nat. Mater. **16**, 1090 (2017).

[16] J.-X. Yin, S. S. Zhang, G. Chang, Q. Wang, S. S. Tsirkin, Z. Guguchia, B. Lian, H. Zhou, K. Jiang, I. Belopolski, N. Shumiya, D. Multer, M. Litskevich, T. A. Cochran, H. Lin, Z. Wang, T. Neupert, S. Jia, H. Lei, and M. Z. Hasan, Negative flat band magnetism in a spin–orbit-coupled correlated kagome magnet, Nat. Phys. **15**, 443 (2019).

[17] J.-X. Yin, W. Ma, T. A. Cochran, X. Xu, S. S. Zhang, H.-J. Tien, N. Shumiya, G. Cheng, K. Jiang, B. Lian, Z. Song, G. Chang, I. Belopolski, D. Multer, M. Litskevich, Z.-J. Cheng, X. P. Yang, B. Swidler, H. Zhou, H. Lin *et al.*, Quantum-limit Chern topological magnetism in $TbMn_6Sn_6$, Nature (London) **583**, 533 (2020).

[18] M. Li, Q. Wang, G. Wang, Z. Yuan, W. Song, R. Lou, Z. Liu, Y. Huang, Z. Liu, H. Lei, Z. Yin, and S. Wang, Dirac cone, flat band and saddle point in kagome magnet YMn_6Sn_6, Nat. Commun. **12**, 3129 (2021).

[19] B. R. Ortiz, L. C. Gomes, J. R. Morey, M. Winiarski, M. Bordelon, J. S. Mangum, I. W. H. Oswald, J. A. Rodriguez-Rivera, J. R. Neilson, S. D. Wilson, E. Ertekin, T. M. McQueen, and E. S. Toberer, New kagome prototype materials: Discovery of KV_3Sb_5, RbV_3Sb_5, and CsV_3Sb_5, Phys. Rev. Mater. **3**, 094407 (2019).

[20] H. Zhao, H. Li, B. R. Ortiz, S. M. Teicher, T. Park, M. Ye, Z. Wang, L. Balents, S. D. Wilson, and I. Zeljkovic, Cascade of correlated electron states in the kagome superconductor CsV_3Sb_5, Nature (London) **599**, 216 (2021).

[21] H. Chen, H. Yang, B. Hu, Z. Zhao, J. Yuan, Y. Xing, G. Qian, Z. Huang, G. Li, Y. Ye, S. Ma, S. Ni, H. Zhang, Q. Yin, C. Gong, Z. Tu, H. Lei, H. Tan, S. Zhou, C. Shen *et al.*, Roton pair density wave in a strong-coupling kagome superconductor, Nature (London) **599**, 222 (2021).

[22] B. R. Ortiz, S. M. L. Teicher, Y. Hu, J. L. Zuo, P. M. Sarte, E. C. Schueller, A. M. Milinda Abeykoon, M. J. Krogstad, S. Rosenkranz, R. Osborn, R. Seshadri, L. Balents, J. He, and S. D. Wilson, CsV_3Sb_5: A z_2 Topological Kagome Metal with a Superconducting Ground State, Phys. Rev. Lett. **125**, 247002 (2020).

[23] Y.-X. Jiang, J.-X. Yin, M. M. Denner, N. Shumiya, B. R. Ortiz, G. Xu, Z. Guguchia, J. He, M. S. Hossain, X. Liu, J. Ruff, L. Kautzsch, S. S. Zhang, G. Chang, I. Belopolski, Q. Zhang, T. A. Cochran, D. Multer, M. Litskevich, Z.-J. Cheng *et al.*, Unconventional chiral charge order in kagome superconductor KV_3Sb_5, Nat. Mater. **20**, 1353 (2021).

[24] C. Mielke III, D. Das, J.-X. Yin, H. Liu, R. Gupta, Y.-X. Jiang, M. Medarde, X. Wu, H. C. Lei, J. Chang, P. Dai, Q. Si, H. Miao, R. Thomale, T. Neupert, Y. Shi, R. Khasanov, M. Z. Hasan, H. Luetkens, and Z. Guguchia, Time-reversal symmetry-breaking charge order in a kagome superconductor, Nature (London) **602**, 245 (2022).

[25] M. M. Denner, R. Thomale, and T. Neupert, Analysis of Charge Order in the Kagome Metal AV_3Sb_5 (A= K, Rb, Cs), Phys. Rev. Lett. **127**, 217601 (2021).

[26] Y.-P. Lin and R. M. Nandkishore, Complex charge density waves at Van Hove singularity on hexagonal lattices: Haldane-model phase diagram and potential realization in the kagome metals AV_3Sb_5 (A=K, Rb, Cs), Phys. Rev. B **104**, 045122 (2021).

[27] L. Nie, K. Sun, W. Ma, D. Song, L. Zheng, Z. Liang, P. Wu, F. Yu, J. Li, M. Shan, D. Zhao, S. Li, B. Kang, Z. Wu, Y. Zhou, K. Liu, Z. Xiang, J. Ying, Z. Wang, T. Wu *et al.*,

Charge-density-wave-driven electronic nematicity in a kagome superconductor, Nature (London) **604**, 59 (2022).

[28] H. Li, T. T. Zhang, T. Yilmaz, Y. Y. Pai, C. E. Marvinney, A. Said, Q. W. Yin, C. S. Gong, Z. J. Tu, E. Vescovo, C. S. Nelson, R. G. Moore, S. Murakami, H. C. Lei, H. N. Lee, B. J. Lawrie, and H. Miao, Observation of Unconventional Charge Density Wave Without Acoustic Phonon Anomaly in Kagome SuperconduCtors AV_3Sb_5 (A=Rb, Cs), Phys. Rev. X **11**, 031050 (2021).

[29] T. Neupert, M. M. Denner, J.-X. Yin, R. Thomale, and M. Z. Hasan, Charge order and superconductivity in kagome materials, Nat. Phys. **18**, 137 (2022).

[30] F. Yu, D. Ma, W. Zhuo, S. Liu, X. Wen, B. Lei, J. Ying, and X. Chen, Unusual competition of superconductivity and charge-density-wave state in a compressed topological kagome metal, Nat. Commun. **12**, 3645 (2021).

[31] Y. Xiang, Q. Li, Y. Li, W. Xie, H. Yang, Z. Wang, Y. Yao, and H.-H. Wen, Twofold symmetry of c-axis resistivity in topological kagome superconductor CsV_3Sb_5 with in-plane rotating magnetic field, Nat. Commun. **12**, 6727 (2021).

[32] J. Ge, P. Wang, Y. Xing, Q. Yin, H. Lei, Z. Wang, and J. Wang, Discovery of charge-4e and charge-6e superconductivity in kagome superconductor CsV_3Sb_5, arXiv:2201.10352.

[33] L. Zheng, Z. Wu, Y. Yang, L. Nie, M. Shan, K. Sun, D. Song, F. Yu, J. Li, D. Zhao, S. Li, B. Kang, Y. Zhou, K. Liu, Z. Xiang, J. Ying, Z. Wang, T. Wu, and X. Chen, Emergent charge order in pressurized kagome superconductor CsV_3Sb_5, Nature (London) **611**, 682 (2022).

[34] X. Feng, K. Jiang, Z. Wang, and J. Hu, Chiral flux phase in the Kagome superconductor AV_3Sb_5, Sci. Bull. **66**, 1384 (2021).

[35] K. Jiang, T. Wu, J.-X. Yin, Z. Wang, M. Z. Hasan, S. D. Wilson, X. Chen, and J. Hu, Kagome superconductors AV_3Sb_5 (A= K, Rb, Cs), Natl. Sci. Rev. **10**, nwac199 (2023).

[36] S.-Y. Yang, Y. Wang, B. R. Ortiz, D. Liu, J. Gayles, E. Derunova, R. Gonzalez-Hernandez, L. Šmejkal, Y. Chen, S. S. Parkin *et al.*, Giant, unconventional anomalous hall effect in the metallic frustrated magnet candidate, KV_3Sb_5, Sci. Adv. **6**, eabb6003 (2020).

[37] A. Subedi, Hexagonal-to-base-centered-orthorhombic 4Q charge density wave order in kagome metals KV_3Sb_5, RbV_3Sb_5, and CsV_3Sb_5, Phys. Rev. Mater. **6**, 015001 (2022).

[38] J. Zhao, W. Wu, Y. Wang, and S. A. Yang, Electronic correlations in the normal state of the kagome superconductor KV_3Sb_5, Phys. Rev. B **103**, L241117 (2021).

[39] H. Tan, Y. Liu, Z. Wang, and B. Yan, Charge Density Waves and Electronic Properties of Superconducting Kagome Metals, Phys. Rev. Lett. **127**, 046401 (2021).

[40] J.-F. Zhang, K. Liu, and Z.-Y. Lu, First-principles study of the double dome superconductivity in the kagome material CsV_3Sb_5 under pressure, Phys. Rev. B **104**, 195130 (2021).

[41] J.-G. Si, W.-J. Lu, Y.-P. Sun, P.-F. Liu, and B.-T. Wang, Charge density wave and pressure-dependent superconductivity in the kagome metal CsV_3Sb_5: A first-principles study, Phys. Rev. B **105**, 024517 (2022).

[42] Z. Liu, M. Li, Q. Wang, G. Wang, C. Wen, K. Jiang, X. Lu, S. Yan, Y. Huang, D. Shen, J.-X. Yin, Z. Wang, Z. Yin, H. Lei, and S. Wang, Orbital-selective Dirac fermions and extremely flat bands in frustrated kagome-lattice metal CoSn, Nat. Commun. **11**, 4002 (2020).

[43] M. Kang, S. Fang, L. Ye, H. C. Po, J. Denlinger, C. Jozwiak, A. Bostwick, E. Rotenberg, E. Kaxiras, J. G. Checkelsky, and R. Comin, Topological flat bands in frustrated kagome lattice CoSn, Nat. Commun. **11**, 4004 (2020).

[44] X. Teng, J. S. Oh, H. Tan, L. Chen, J. Huang, B. Gao, J.-X. Yin, J.-H. Chu, M. Hashimoto, D. Lu, C. Jozwiak, A. Bostwick, E. Rotenberg, G. E. Granroth, B. Yan, R. J. Birgeneau, P. Dai, and M. Yi, Intertwined magnetism and charge density wave order in kagome FeGe, Nat. Phys. **19**, 814 (2023).

[45] X. Teng, L. Chen, F. Ye, E. Rosenberg, Z. Liu, J.-X. Yin, Y.-X. Jiang, J. S. Oh, M. Z. Hasan, K. J. Neubauer, B. Gao, Y. Xie, M. Hashimoto, D. Lu, C. Jozwiak, A. Bostwick, E. Rotenberg, R. J. Birgeneau, J.-H. Chu, M. Yi *et al.*, Discovery of charge density wave in a kagome lattice antiferromagnet, Nature (London) **609**, 490 (2022).

[46] J.-X. Yin, Y.-X. Jiang, X. Teng, M. S. Hossain, S. Mardanya, T.-R. Chang, Z. Ye, G. Xu, M. M. Denner, T. Neupert, B. Lienhard, H.-B. Deng, C. Setty, Q. Si, G. Chang, Z. Guguchia, B. Gao, N. Shumiya, Q. Zhang, T. A. Cochran *et al.*, Discovery of Charge Order and COrresponding Edge State in Kagome Magnet FeGe, Phys. Rev. Lett. **129**, 166401 (2022).

[47] C. Setty, C. A. Lane, L. Chen, H. Hu, J.-X. Zhu, and Q. Si, Electron correlations and charge density wave in the topological kagome metal FeGe, arXiv:2203.01930.

[48] S. Shao, J.-X. Yin, I. Belopolski, J.-Y. You, T. Hou, H. Chen, Y.-X. Jiang, M. S. Hossain, M. Yahyavi, C.-H. Hsu, Y. Feng, A. Bansil, M. Z. Hasan, and G. Chang, Intertwining of magnetism and charge ordering in kagome FeGe, ACS Nano **17**, 10164 (2023).

[49] H. Miao, T. T. Zhang, H. X. Li, G. Fabbris, A. H. Said, R. Tartaglia, T. Yilmaz, E. Vescovo, S. Murakami, L. X. Feng, K. Jiang, X. L. Wu, A. F. Wang, S. Okamoto, Y. L. Wang, and H. N. Lee, Charge dimerization in strongly correlated kagome magnet FeGe, arXiv:2210.06359.

[50] T. Ohoyama, K. Kanematsu, and K. Yasukōchi, A new intermetallic compound FeGe, J. Phys. Soc. Jpn. **18**, 589 (1963).

[51] O. Beckman, K. Carrander, L. Lundgren, and M. Richardson, Susceptibility measurements and magnetic ordering of hexagonal FeGe, Phys. Scr. **6**, 151 (1972).

[52] L. Häggström, T. Ericsson, R. Wäppling, and E. Karlsson, Mössbauer study of hexagonal fege, Phys. Scr. **11**, 55 (1975).

[53] U. Gäfvert, L. Lundgren, B. Westerstrandh, and O. Beckman, Crystalline anisotropy energy of uniaxial antiferromagnets evaluated from low field torque data, J. Phys. Chem. Solids **38**, 1333 (1977).

[54] J. Forsyth, C. Wilkinson, and P. Gardner, The low-temperature magnetic structure of hexagonal FeGe, J. Phys. F **8**, 2195 (1978).

[55] J. Bernhard, B. Lebech, and O. Beckman, Neutron diffraction studies of the low-temperature magnetic structure of hexagonal FeGe, J. Phys. F **14**, 2379 (1984).

[56] J. Bernhard, B. Lebech, and O. Beckman, Magnetic phase diagram of hexagonal FeGe determined by neutron diffraction, J. Phys. F **18**, 539 (1988).

[57] H. Chen, Q. Niu, and A. H. MacDonald, Anomalous Hall Effect Arising from Noncollinear Antiferromagnetism, Phys. Rev. Lett. **112**, 017205 (2014).

[58] T. Suzuki, R. Chisnell, A. Devarakonda, Y.-T. Liu, W. Feng, D. Xiao, J. W. Lynn, and J. Checkelsky, Large anomalous Hall

effect in a half-Heusler antiferromagnet, Nat. Phys. **12**, 1119 (2016).
[59] S. Nakatsuji, N. Kiyohara, and T. Higo, Large anomalous Hall effect in a non-collinear antiferromagnet at room temperature, Nature (London) **527**, 212 (2015).
[60] F. Kekulé, Studies on aromatic compounds, Ann. Chemie Pharm., Leipzig **137**, 129 (1866).
[61] A. I. Liechtenstein, M. Katsnelson, V. Antropov, and V. Gubanov, Local spin density functional approach to the theory of exchange interactions in ferromagnetic metals and alloys, J. Magn. Magn. Mater. **67**, 65 (1987).
[62] X. Wan, Q. Yin, and S. Y. Savrasov, Calculation of Magnetic Exchange Interactions in Mott-Hubbard Systems, Phys. Rev. Lett. **97**, 266403 (2006).
[63] X. Wan, T. A. Maier, and S. Y. Savrasov, Calculated magnetic exchange interactions in high-temperature superconductors, Phys. Rev. B **79**, 155114 (2009).
[64] A. R. Mackintosh and O. K. Andersen, *Electrons at the Fermi Surface*, edited by M. Springford (Cambridge University Press, Cambridge, England, 1980).
[65] M. Weinert, R. E. Watson, and J. W. Davenport, Total-energy differences and eigenvalue sums, Phys. Rev. B **32**, 2115 (1985).
[66] I. Dzyaloshinsky, A thermodynamic theory of weak ferromagnetism of antiferromagnetics, J. Phys. Chem. Solids **4**, 241 (1958).
[67] T. Moriya, Anisotropic superexchange interaction and weak ferromagnetism, Phys. Rev. **120**, 91 (1960).
[68] P. Blaha, K. Schwarz, G. Madsen, D. Kvasnicka, and J. Luitz, WIEN2K, *An Augmented Plane Wave+ Local Orbitals Program for Calculating Crystal Properties*, edited by K. Schwarz (Vienna University of Technology, Austria, 2001).
[69] G. Kotliar, S. Y. Savrasov, K. Haule, V. S. Oudovenko, O. Parcollet, and C. A. Marianetti, Electronic structure calculations with dynamical mean-field theory, Rev. Mod. Phys. **78**, 865 (2006).
[70] S. H. Vosko, L. Wilk, and M. Nusair, Accurate spin-dependent electron liquid correlation energies for local spin density calculations: A critical analysis, Can. J. Phys. **58**, 1200 (1980).
[71] Y. Du, X. Wan, L. Sheng, J. Dong, and S. Y. Savrasov, Electronic structure and magnetic properties of $NaOsO_3$, Phys. Rev. B **85**, 174424 (2012).
[72] X. Wan, A. M. Turner, A. Vishwanath, and S. Y. Savrasov, Topological semimetal and Fermi-arc surface states in the electronic structure of pyrochlore iridates, Phys. Rev. B **83**, 205101 (2011).
[73] X. Wan, A. Vishwanath, and S. Y. Savrasov, Computational Design of Axion Insulators Based on 5*d* Spinel Compounds, Phys. Rev. Lett. **108**, 146601 (2012).
[74] A. Dussaux, P. Schoenherr, K. Koumpouras, J. Chico, K. Chang, L. Lorenzelli, N. Kanazawa, Y. Tokura, M. Garst, A. Bergman, C. L. Degen, and D. Meier, Local dynamics of topological magnetic defects in the itinerant helimagnet FeGe, Nat. Commun. **7**, 12430 (2016).
[75] V. Guritanu, D. van der Marel, J. Teyssier, T. Jarlborg, H. Wilhelm, M. Schmidt, and F. Steglich, Optical evidence for heavy charge carriers in FeGe, Phys. Rev. B **75**, 155114 (2007).
[76] S. Grytsiuk and S. Blügel, Micromagnetic description of twisted spin spirals in the B20 chiral magnet FeGe from first principles, Phys. Rev. B **104**, 064420 (2021).
[77] V. I. Anisimov, F. Aryasetiawan, and A. I. Lichtenstein, First-principles calculations of the electronic structure and spectra of strongly correlated systems: the LDA+U method, J. Phys.: Condens. Matter **9**, 767 (1997).
[78] D. D. Koelling and B. N. Harmon, A technique for relativistic spin-polarised calculations, J. Phys. C **10**, 3107 (1977).
[79] X. Wan, J. Dong, and S. Y. Savrasov, Mechanism of magnetic exchange interactions in europium monochalcogenides, Phys. Rev. B **83**, 205201 (2011).
[80] X. Wan, V. Ivanov, G. Resta, I. Leonov, and S. Y. Savrasov, Exchange interactions and sensitivity of the Ni two-hole spin state to Hund's coupling in doped $NdNiO_2$, Phys. Rev. B **103**, 075123 (2021).
[81] D. Wang, X. Bo, F. Tang, and X. Wan, Calculated magnetic exchange interactions in the Dirac magnon material Cu_3TeO_6, Phys. Rev. B **99**, 035160 (2019).
[82] N. Metropolis and S. Ulam, The Monte Carlo method, J. Am. Stat. Assoc. **44**, 335 (1949).
[83] Z.-X. Shen, C. Su, and L. He, High-throughput computation and structure prototype analysis for two-dimensional ferromagnetic materials, npj Comput. Mater **8**, 132 (2022).
[84] K. Cao, G.-C. Guo, D. Vanderbilt, and L. He, First-principles Modeling of Multiferroic $R\mathrm{Mn_2O_5}$, Phys. Rev. Lett. **103**, 257201 (2009).
[85] https://github.com/diwang0214/FeGe.
[86] P. Baral, N. Ahmed, J. Kumar, S. Nair, and R. Nath, Synthesis and physical properties of spin-1 honeycomb lattice $Pb_6Ni_9(TeO_6)_5$, J. Alloys Compd. **711**, 568 (2017).
[87] R. Chisnell, J. S. Helton, D. E. Freedman, D. K. Singh, R. I. Bewley, D. G. Nocera, and Y. S. Lee, Topological Magnon Bands in a Kagome Lattice Ferromagnet, Phys. Rev. Lett. **115**, 147201 (2015).
[88] T. Holstein and H. Primakoff, Field dependence of the intrinsic domain magnetization of a ferromagnet, Phys. Rev. **58**, 1098 (1940).
[89] D. Wang, J. Yu, F. Tang, Y. Li, and X. Wan, Determination of the range of magnetic interactions from the relations between magnon eigenvalues at high-symmetry κ points, Chin. Phys. Lett. **38**, 117101 (2021).
[90] C. J. Bradley and A. P. Cracknell, *The Mathematical Theory of Symmetry in Solids: Representation Theory for Point Groups and Space Groups* (Oxford University Press, Oxford, 1972).
[91] J. P. Perdew, K. Burke, and M. Ernzerhof, Generalized Gradient Approximation Made Simple, Phys. Rev. Lett. **77**, 3865 (1996).
[92] J. P. Perdew and Y. Wang, Accurate and simple analytic representation of the electron-gas correlation energy, Phys. Rev. B **45**, 13244 (1992).
[93] Z. Wu and R. E. Cohen, More accurate generalized gradient approximation for solids, Phys. Rev. B **73**, 235116 (2006).
[94] J. P. Perdew, A. Ruzsinszky, G. I. Csonka, O. A. Vydrov, G. E. Scuseria, L. A. Constantin, X. Zhou, and K. Burke, Restoring the Density-Gradient Expansion for Exchange In Solids And Surfaces, Phys. Rev. Lett. **100**, 136406 (2008).